Supplementary Information

LnDOTA puppeteering: removing the water molecule and imposing tetragonal symmetry

Anna S. Manvell[a£], Rouven Pfleger[a,b£€], Niels A. Bonde[a,c], Matteo Briganti[d], Carlo Andrea Mattei[d], Theis Brock Nannestad[a], Høgni Weihe[a], Annie K. Powell[b], Jacques Ollivier[c], Jesper Bendix[a], Mauro Perfetti[d]

Affiliations

[a]Department of Chemistry, University of Copenhagen, Universitetsparken 5, DK-2100 Copenhagen, Denmark.

[b]Institute of Inorganic Chemistry, Karlsruhe Institute of Technology, Engesserstrasse 15, 76131 Karlsruhe (Germany)

[c]Institut Laue-Langevin, 71 avenue des Martyrs, CS 20156, 38042 Grenoble Cedex 9, France

[d]Department of Chemistry U. Schiff, Via della Lastruccia 3, 50019, Sesto Fiorentino, Italy.

[£]These authors have equally contributed to this work.

[€]Current address: Department of Biological and Chemical Engineering, Åbogade 40, 8200 Aarhus N, Denmark.

INDEX

1. Synthesis and chemical characterization S3

2. Ab initio calculations S6

3. Crystal Field Parameters from fit S7

4. Inelastic Neutron Scattering S8

5. Luminescence spectroscopy S10

6. EPR S13

7. Magnetic measurements: M vs T S15

8. Energy level splitting and composition S18

9. Magnetic measurements: M vs H S23

10. Nephelauxetic effects S25

11. Anisotropy of the complexes S28

12. Ac measurements S29

1. Synthesis and chemical characterization

The synthesis of **Y** is reported in detail. The same procedure was followed for the synthesis of the other compounds.

[Me_4N][YDOTA]·2Me_4NCl·5H_2O (Y). H_4DOTA (210 mg, 0.52 mmol) and $YCl_3·6H_2O$ (152 mg, 0.50 mmol) were dissolved in water (4 mL). After heating up to 80°C, a solution of $Me_4NOH·5H_2O$ (373 mg, 2.1 mmol) in water (0.5 ml) was added dropwise. The obtained suspension was then filtered, and a solution of Me_4NCl (583 mg, 5.3 mmol) in water (1 ml) was added to the filtrate. The resultant solution was allowed to slowly concentrate at ca. 50°C, and after few hours to few days needle shaped crystals suitable for single crystal X-ray diffraction studies were obtained. The product was washed with either cold water or isopropanol to remove Me_4NCl, which co-precipitated. Crystals were placed on a filter paper and transferred in a vial when dry. Anal Calcd for $C_{28}H_{70}Cl_2N_7O_{13}Y$: C, 38.54; H, 8.08; N, 11.23. Found: C, 38.0; H, 7.88; N, 11.30. The purity of the crystalline phase was checked by powder X-ray diffraction analysis (Figure S1). The product appeared stable over time, without requiring any particular attention for its conservation. However, for periods longer than a few weeks, crystals were stored in a desiccator containing $CoCl_2$.

[Me_4N][TbDOTA]·2Me_4NCl·5H_2O (Tb). H_4DOTA (209 mg, 0.52 mmol), $TbCl_3·6H_2O$ (187 mg, 0.50 mmol), $Me_4NOH·5H_2O$ (378 mg, 2.1 mmol), Me_4NCl (562 mg, 5.1 mmol). Anal Calcd for $C_{28}H_{70}Cl_2N_7O_{13}Tb$: C, 35.67; H, 7.48; N, 10.40. Found: C, 36.1; H, 7.54; N, 10.10.

[Me_4N][DyDOTA]·2Me_4NCl·5H_2O (Dy). H_4DOTA (210 mg, 0.52 mmol), $DyCl_3·6H_2O$ (196 mg, 0.52 mmol), $Me_4NOH·5H_2O$ (377 mg, 2.1 mmol), Me_4NCl (570 mg, 5.2 mmol). Anal Calcd for $C_{28}H_{70}Cl_2DyN_7O_{13}$: C, 35.54; H, 7.46; N, 10.36. Found: C, 36.4; H, 7.83; N, 10.30.

[Me_4N][HoDOTA]·2Me_4NCl·5H_2O (Ho). H_4DOTA (209 mg, 0.52 mmol), $HoCl_3·6H_2O$ (188 mg, 0.50 mmol), $Me_4NOH·5H_2O$ (373 mg, 2.1 mmol), Me_4NCl (566 mg, 5.2 mmol). Anal Calcd for $C_{28}H_{70}Cl_2HoN_7O_{13}$: C, 35.45; H, 7.44; N, 10.33. Found: C, 36.4; H, 7.90; N, 10.30.

[Me_4N][ErDOTA]·2Me_4NCl·5H_2O (Er). H_4DOTA (210 mg, 0.52 mmol), $ErCl_3·6H_2O$ (192 mg, 0.50 mmol), $Me_4NOH·5H_2O$ (372 mg, 2.1 mmol), Me_4NCl (555 mg, 5.1 mmol). Anal Calcd for $C_{28}H_{70}Cl_2ErN_7O_{13}$: C, 35.36; H, 7.42; N, 10.31. Found: C, 36.5; H, 7.95; N, 10.50.

[Me_4N][TmDOTA]·2Me_4NCl·5H_2O (Tm). H_4DOTA (210 mg, 0.52 mmol), $TmCl_3·6H_2O$ (192 mg, 0.50 mmol), $Me_4NOH·5H_2O$ (373 mg, 2.0 mmol), Me_4NCl (559 mg, 5.1 mmol). Anal Calcd for $C_{28}H_{70}Cl_2N_7O_{13}Tm$: C, 35.30; H, 7.41; N, 10.29. Found: C, 35.9; H, 7.43; N, 10.40.

[Me_4N][YbDOTA]·2Me_4NCl·5H_2O (Yb). H_4DOTA (210 mg, 0.52 mmol), $YbCl_3·6H_2O$ (195 mg, 0.50 mmol), $Me_4NOH·5H_2O$ (376 mg, 2.1 mmol), Me_4NCl (570 mg, 5.2 mmol). Anal Calcd for $C_{28}H_{70}Cl_2N_7O_{13}Yb$: C, 35.15; H, 7.37; N, 10.25. Found: C, 35.6; H, 7.65; N, 10.20.

Compound	Y	Tb	Dy	Ho	Er	Tm	Yb
Crystal system	Tetragonal	Tetragonal	Tetragonal	Tetragonal	Tetragonal	Tetragonal	Tetragonal
Space group	P4bm (No. 100)	P4bm (No. 100)	P4bm (No. 100)	P4bm (No. 100)	P4bm (No. 100)	P4bm (No. 100)	P4bm (No. 100)
a / Å	17.4345(6)	17.4148(6)	17.4527(9)	17.4077(7)	17.4237(9)	17.3929(6)	17.3928(6)
b / Å	17.4345(6)	17.4148(6)	17.4527(9)	17.4077(7)	17.4237(9)	17.3929(6)	17.3928(6)
c / Å	6.7946(3)	6.7819(4)	6.7995(4)	6.7730(4)	6.7843(5)	6.7672(4)	6.7688(3)
α,β,γ / °	90	90	90	90	90	90	90
V / Å^3	2065.30(17)	2056.78(19)	2071.1(2)	2052.4(2)	2059.6(3)	2047.17(19)	2047.63(17)
Z	2	4	18	4	2	4	4
T / K	296	296	296	296	296	296	296
$\rho_{\chi\omega\lambda\chi}$ / γ.χμ^{-3}	1.424	1.546	1.528	1.563	1.446	1.557	1.566
μ / mm^{-1}	1.609	1.917	2	2.126	2.231	2.365	2.482
F(000)	938	994	979	1002	863	986	992
λ Radiation / Å	0.71073	0.71073	0.71073	0.71073	0.71073	0.71073	0.71073
2θ range / °	3.30 ≤ 2θ ≤ 51.26	4.68 ≤ 2θ ≤ 65.15	5.22 ≤ 2θ ≤ 54.97	4.68 ≤ 2θ ≤ 65.15	4.68 ≤ 2θ ≤ 65.14	4.68 ≤ 2θ ≤ 69.93	3.31 ≤ 2θ ≤ 54.17
Number of reflections	30819	51344	22787	43892	47893	49189	41528
Indep.reflections	2068	3910	2466	3892	3912	4595	2375
R_{int}, R_σ	0.0823, 0.0312	0.0489, 0.0272	0.0298, 0.0228	0.0633, 0.0343	0.0463, 0.0272	0.0584, 0.0386	0.0493, 0.0178
Parameters / Restrains	152 / 1	155 / 1	150 / 1	152 / 1	148 / 1	142 / 1	148 / 1
S (on F^2)	1.038	1.119	1.116	1.093	1.098	1.062	1.194
R_1, wR_2 (I ≥ 4σ)	0.0459, 0.1221	0.0195, 0.0439	0.0169, 0.0414	0.0220, 0.0490	0.0178, 0.0386	0.0255, 0.0561	0.0224, 0.0774
R_1 (all data)	0.0529	0.0294	0.0188	0.0354	0.0264	0.0435	0.0305
$\Delta\rho_{max}$ / $\Delta\rho_{min}$ / e·Å^{-3}	0.396 / -0.550	0.655 / -0.589	0.647 / -0.818	0.676 / -0.522	0.378 / -0.427	2.262 / -0.577	0.713 / -0.791
Flack parameter	0.401(3)	0.001(5)	0.007(5)	0.016(6)	0.007(4)	0.017(6)	0.371(4)
CCDC deposit #	2281620	2281617	2281615	2281619	2281616	2281618	2281329

Table S1. Crystallographic data for the synthesized LnDOTA (Ln = Y, Tb, Dy, Ho, Er, Tm and Yb).

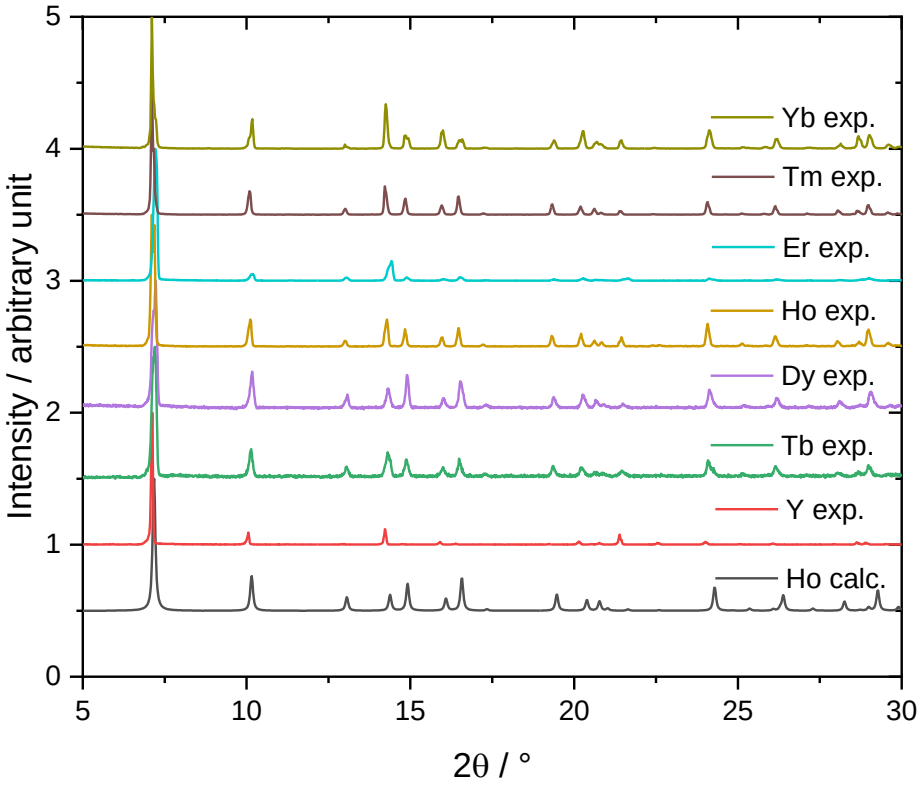

Figure S1. Powder XRD diffractograms of the synthesized compounds.

	Y	Tb	Dy	Ho	Er	Tm	Yb
Ln-O plane/ Å	1.048	1.039	1.044	1.056	1.060	1.059	1.072
		0.721	0.721	0.726	0.727	0.735	0.728
Ln-N plane/ Å	1.499	1.521	1.511	1.492	1.48	1.471	1.464
		1.617	1.619	1.601	1.59	1.587	1.588
Torsion / °	23.84	23.40	23.77	23.83	24.27	23.49	24.51
		38.92	39.23	39.52	39.6	39.76	39.91
Ln-O bond/ Å	2.297	2.319	2.311	2.3	2.289	2.277	2.273
		2.348	2.33	2.33	2.32	2.304	2.29
Ln-N bond/ Å	2.553	2.572	2.562	2.547	2.54	2.531	2.525
		2.652	2.64	2.631	2.625	2.623	2.62
O-Ln-vert / °	62.85	63.39	63.25	62.66	62.40	62.27	61.88
		72.14	72.02	71.85	71.73	71.43	71.51

Table S2. Metrical parameters of **Ln** (this work, orange) and $[LnDOTA{\cdot}H_2O]^-$ (blue)[1].

2. Ab initio calculations

Computational details: All simulations were performed with ORCA 5.0.2 Quantum Chemistry Software Package.[2] Second-order Douglas-Kroll-Hess Hamiltonian was always employed to consider scalar relativistic corrections. SARC2-QZVP basis sets[3] were employed for the lanthanide ion, while DKH-def2[4] basis sets were used for all other atomic species: TZVP for nitrogen and oxygen, SVP for all other atomic species. Resolution of Identity (RI) approximation was applied[5] with the default settings for the integration grids. AUTOAUX feature was used to automatically generate the corresponding auxiliary basis sets. The energy ladder of the electronic states for each lanthanide ion was computed within the CASSCF method followed by Spin Orbit coupling calculations within the Quasi-Degenerate Perturbation Theory (QDPT) and mean field approaches. CASSCF Energies and eigenvectors were corrected by second-order N-electron valence perturbation theory (NEVPT2) to include dynamical correlation effects.[6] The chosen active space for the lanthanides consisted of the unpaired electrons in the seven 4f -orbitals of the lanthanide ion in the oxidation state +3: CAS (N,7), where N is the number of 4f electrons in Ln^{3+} ions. Due to hardware limitations, only the states with the highest spin multiplicity for each lanthanide were computed and included in the following spin-orbit calculation: 7 septuplets for **Tb**, 21 sextuplets for **Dy**, 35 quintuplets for **Ho**, 35 quadruplets for **Er**, 21 triplets for **Tm**, 7 doublets for **Yb**. The g-tensor and the Extended Stevens' Operator (ESO) for each complex were computed with the SINGLE_ANISO module[7, 8] as implemented in ORCA. The quantization axis was always set along the C_4 axis of the molecule.

	B20	B40	B60	B44	B4-4	B64	B6-4
Tb	-1045	-629	935	503	-741	-562	-467
Dy	-1025	-1123	712	461	957	-373	716
Ho	-1051	-840	541	551	-560	810	203
Er	-808	-824	419	612	-401	599	158
Tm	-966	-778	467	134	839	565	476
Yb	-851	-1101	584	795	-204	498	-576

Table S3. Crystal Field parameters (cm^{-1}) extracted from the *ab initio* calculations (Wybourne notation). The conversion between Wybourne (B^k_q) and Stevens (b^k_q) formalism is: $B_q^k = b_q^k/(R \cdot n)$ where *R* is the appropriate reduced matrix element reported in Table 20 of Abragam and Bleaney[9] and *n* is a conversion factor reported in Table A.1 of Stewart.[10]

3. Crystal Field parameters from fit

The CF parameters were fitted using a home-written program in MATLAB. The program used as an input all the magnetometric data (magnetization and χT curves), all the energies obtained from the spectroscopic measurements (luminescence, INS), as well as the *g* factors extracted from EPR. The Hamiltonian reported in the main paper was used to fit all the experimental data for a given Ln ion. The minimization procedure was based on a least square fit implemented in the MINUIT subroutine.

	B20	B40	B44	B60	B64	B6-4
Tb	-891	-203	297	365	385	-300
Dy	-820	-1662	1441	1144	215	-350
Ho	-1319	-1247	632	307	379	-264
Er	-882	-441	1645	626	286	-22
Tm	-752	-441	644	6850	788	-226
Yb	-441	-416	1621	3243	539	-1252

Table S4. Crystal Field parameters (cm^{-1}) extracted from the fit (Wybourne notation). The conversion between Wybourne (B^k_q) and Stevens (b^k_q) formalism is: $B_q^k = b_q^k/(R \cdot n)$ where *R* is the appropriate reduced matrix element reported in Table 20 of Abragam and Bleaney[9] and *n* is a conversion factor reported in Table A.1 of Stewart.[10]

4. Inelastic Neutron Scattering

Experimental: The INS data were recorded at Institut Laue-Langevin, Grenoble, France, using the direct geometry cold and thermal neutron time-of-flight instruments IN5 (project DOI: 10.5291/ILL-DATA.4-06-17). Samples of approximately 1 g were wrapped in aluminum foil and placed in cylindrical aluminium canisters. Using a standard ILL Orange Cryostat, the compounds were measured at selected temperatures and wavelengths. Detector efficiency was corrected for by normalizing the spectra to a standard vanadium sample, and the data set was corrected for absorption, but otherwise the data are presented as obtained. Data reduction, binning, and plotting were performed using a home-made MATLAB script.

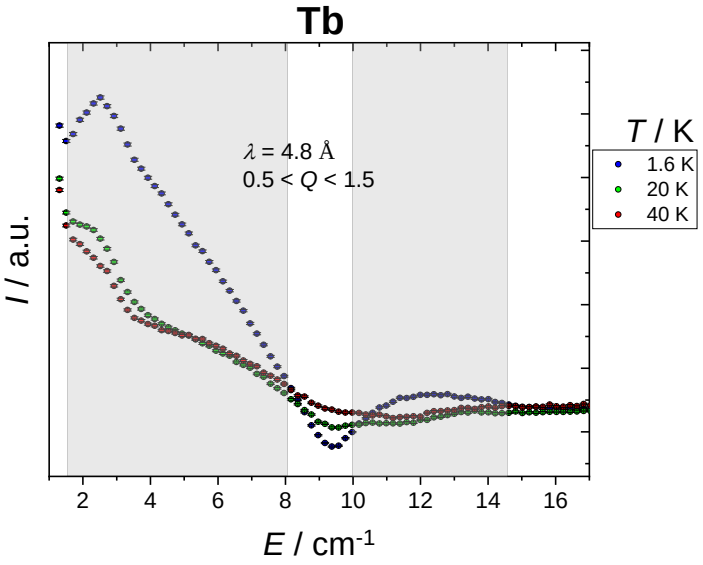

Figure S2. INS spectra of **Tb** measured at incident neutron wavelength λ_i = 4.8 Å at T = 1.6 K, 20 K and 40 K. Spectrum integrated over the following Q-range: 0.5 < Q < 1.5. The grey boxes correspond to regions where the magnetic transitions are present.

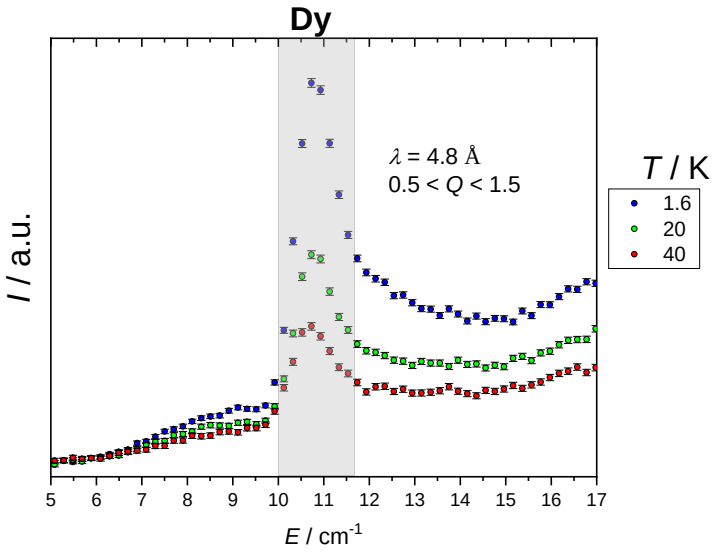

Figure S3. INS spectra of **Dy** measured at incident neutron wavelength λ_i = 4.8 Å at T = 1.6 K, 20 K and 40 K. Spectrum integrated over the following Q-range: 0.5 < Q < 1.5. The grey boxes correspond to regions where the magnetic transitions are present.

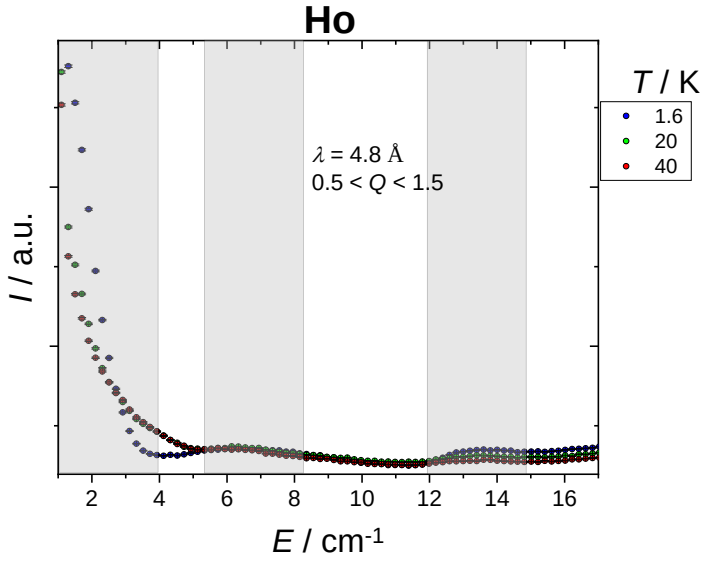

Figure S4. INS spectra of **Ho** measured at incident neutron wavelength λ_i = 4.8 Å at T = 1.6 K, 20 K and 40 K. Spectrum integrated over the following Q-range: 0.5 < Q < 1.5. The grey boxes correspond to regions where the magnetic transitions are present.

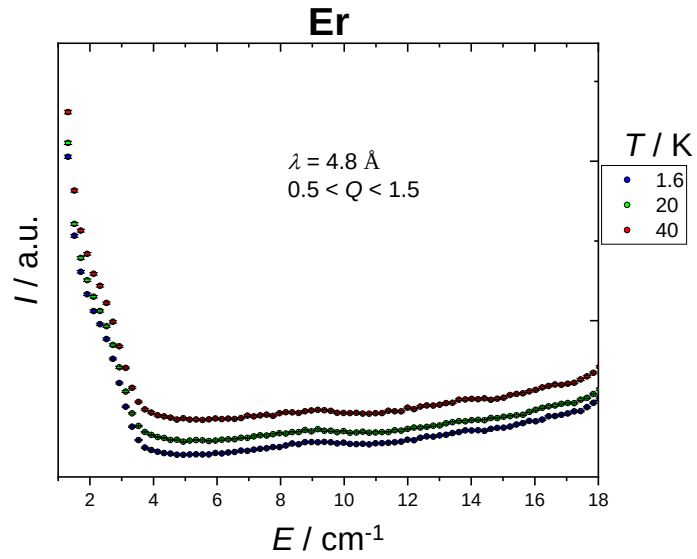

Figure S5. INS spectra of **Er** measured at incident neutron wavelength λ_i = 4.8 Å at T = 1.6 K, 20 K and 40 K. Spectrum integrated over the following Q-range: 0.5 < Q < 1.5. No magnetic transitions are found.

5. Luminescence spectroscopy

Experimental: All luminescence measurements were carried out on a Horiba Fluorolog spectrofluorometer. The FlourEssence v3.5 software was used to acquire the data. Before measuring, the samples were crushed (approximately 50 mg per sample) to a fine powder and mixed with grease. The greasy powder was smeared onto a piece of black cardboard.

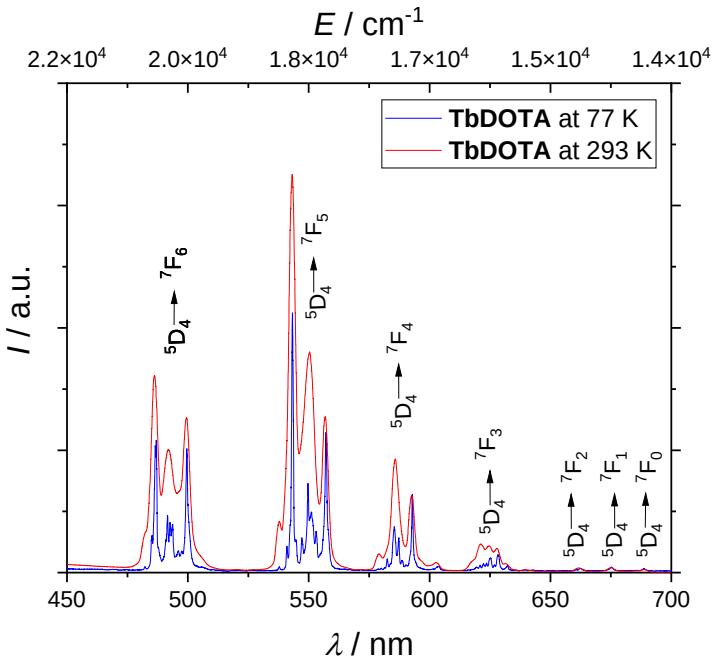

Figure S6. Solid state luminescence spectrum of **Tb**. Blue line: 77 K, red line: room temperature. Excitation wavelength: 380 nm.

RS multiplet	Baricentre / cm^{-1}
$^7F_6$	0
$^7F_5$	2500
$^7F_4$	3750
$^7F_3$	4500
$^7F_2$	5500
$^7F_1$	5700
$^7F_0$	5800

Table S5. Experimentally measured baricentres of the RS multiplet of **Tb**. The energy was arbitrarily scaled to have the first multiplet at E = 0.

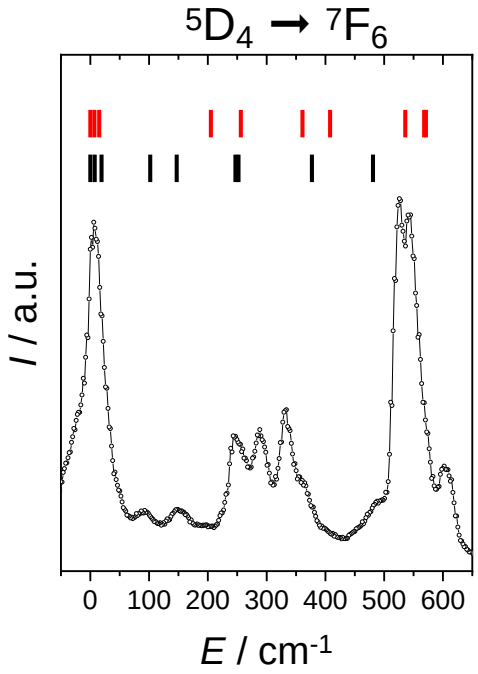

Figure S7. Zoom on the ground multiplet of **Tb**. The energy was arbitrarily scaled to have the first peak at E = 0. The black and red ticks on the figure represent the energies obtained from the fit and the ab initio calculations, respectively.

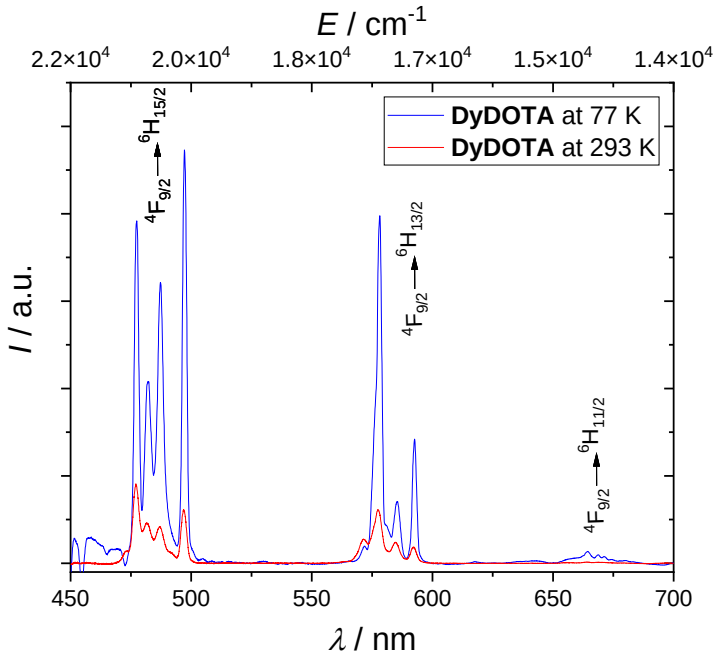

Figure S8. Solid state luminescence spectrum of **Dy**. Blue line: 77 K, red line: room temperature. Excitation wavelength: 380 nm.

RS multiplet	Baricentre / cm^{-1}
$^6H_{15/2}$	0
$^6H_{13/2}$	4300
$^6H_{11/2}$	6000

Table S6. Experimentally measured baricentres of the RS multiplet of **Dy**. The energy was arbitrarily scaled to have the first multiplet at E = 0.

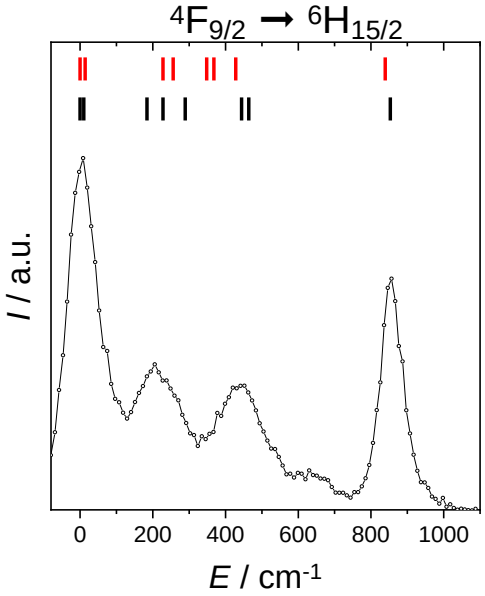

Figure S9. Zoom on the ground multiplet of **Dy**. The energy was arbitrarily scaled to have the first peak at E = 0. The black and red ticks on the figure represent the energies obtained from the fit and the ab initio calculations, respectively.

6. EPR

Experimental: The X-band EPR measurements were obtained on crystalline powders at *T* = 4 K on **LnY** samples (Ln = Dy, Er, Yb; 2% Ln 98% Y).

The simulations were obtained using an effective S = ½ ground state with *g* values extracted from either the fitted CF parameters or from the *ab initio* calculated CF parameters. The inclusion of an hyperfine term to the Hamiltonian was used to reproduce the fine structure of the spectra.

$$\mathcal{H} = \mu_B \hat{\boldsymbol{S}} \cdot \bar{\bar{\boldsymbol{g}}} \cdot \boldsymbol{B} + \hat{\boldsymbol{S}} \cdot \bar{\bar{\boldsymbol{A}}} \cdot \hat{\boldsymbol{I}}$$

	Ground *g* components ($g_\perp$, $g_{//}$)			A components ($A_\perp$, $A_{//}$) / cm^{-1}	Broadening / G
	Exp	Fit	*Ab initio*		
Dy	9.46, -	9.97, 1.03	10.0, 0.464	0.037, 0	45
Er	3.52, 11.58	3.51, 12.3	3.38, 11.88	0, 0.2	10
Yb	2.89, 4.22	2.85, 4.32	2.82, 4.34	0.021, 0.03	30

Table S7. Parameters used for the EPR simulations. The *g* values were fixed to the ones obtained from the CF parameters.

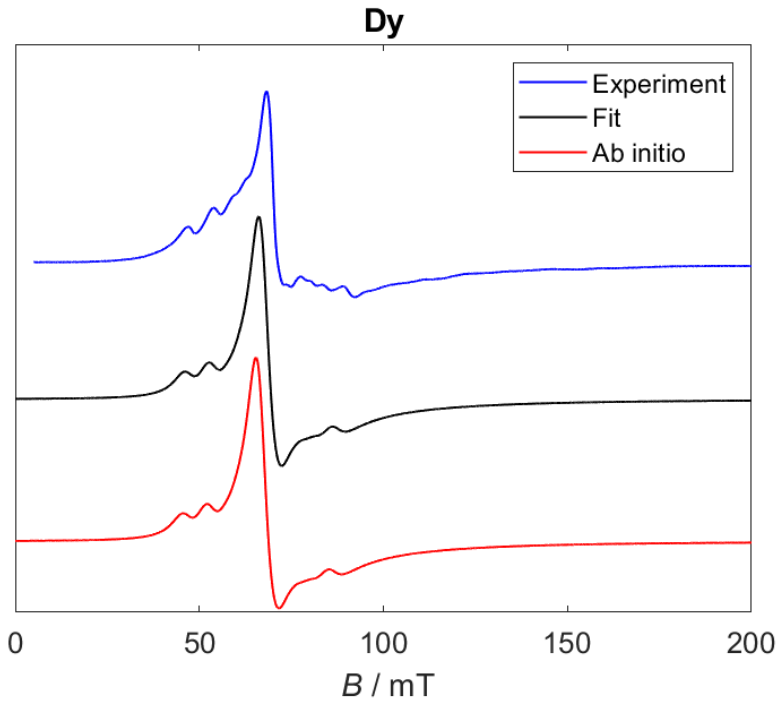

Figure S10. Experimental (blue trace), fitted (black trace) and *ab initio* calculated (red trace) X-band EPR spectrum of **DyY**.

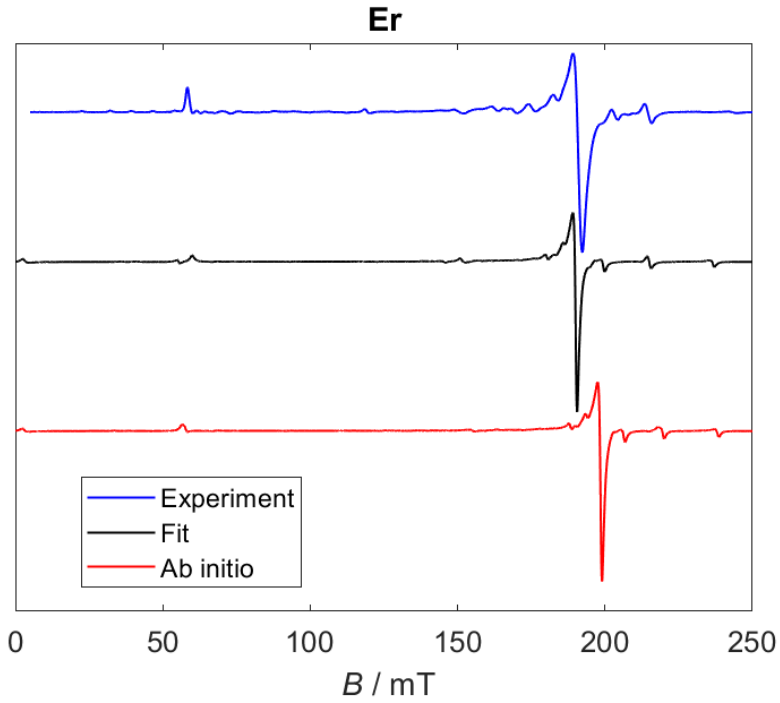

Figure S11. Experimental (blue trace), fitted (black trace) and *ab initio* calculated (red trace) X-band EPR spectrum of **ErY**.

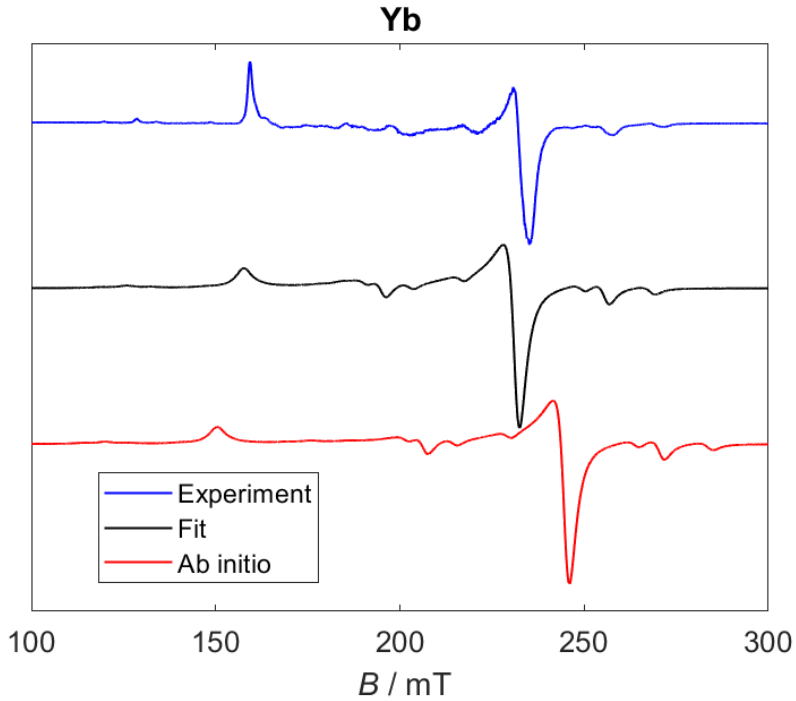

Figure S12. Experimental (blue trace), fitted (black trace) and *ab initio* calculated (red trace) X-band EPR spectrum of **YbY**.

7. Magnetic measurements: magnetic moment vs temperature

Experimental: All magnetic measurements were carried out on a Quantum Design MPMS-XL SQUID magnetometer equipped with a 50000 Oe dc magnet. Before measuring, the samples were crushed (approximately 50 mg per sample) to a fine powder and put in a polycarbonate capsule. Before the capsule was sealed, approximately 20 mg hexadecane was added to prevent the sample from orienting with the field during the measurement. Diamagnetism was corrected using Pascal's constants.

	Curie constant	Experimental χT	Fitted χT	Calculated χT
Tb	11.82	11.78	11.73	11.59
Dy	14.17	14.02	13.88	13.90
Ho	14.07	13.61	13.92	13.73
Er	11.48	11.05	11.26	11.26
Tm	7.15	5.50	5.83	6.88
Yb	2.57	1.88	2.05	2.30

Table S8. Comparison between experimental, fitted and calculated room temperature χT values (H = 1000 Oe). All values are reported in emu K mol^{-1}.

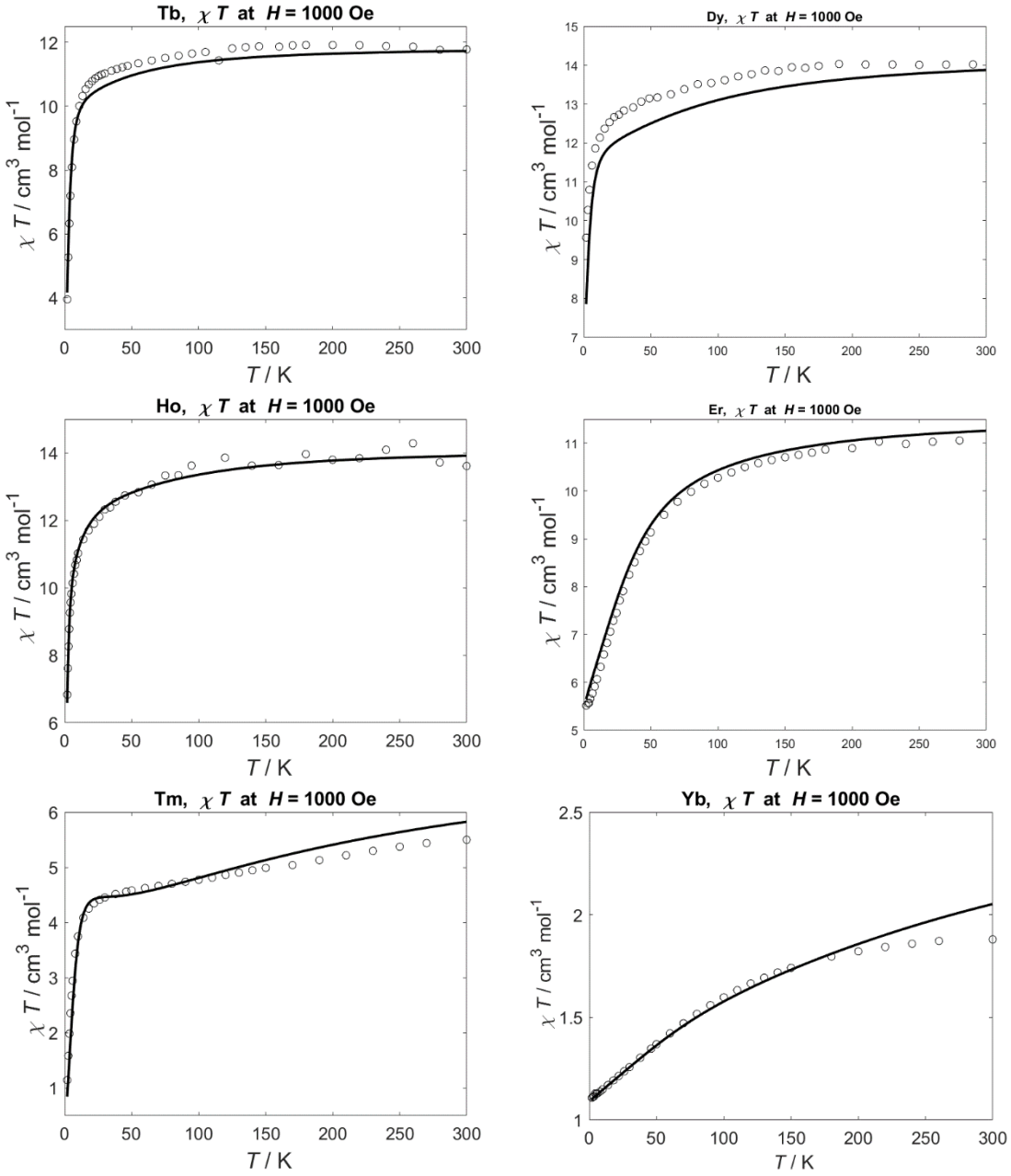

Figure S13. χT vs T curves (symbols) and best fit (black lines).

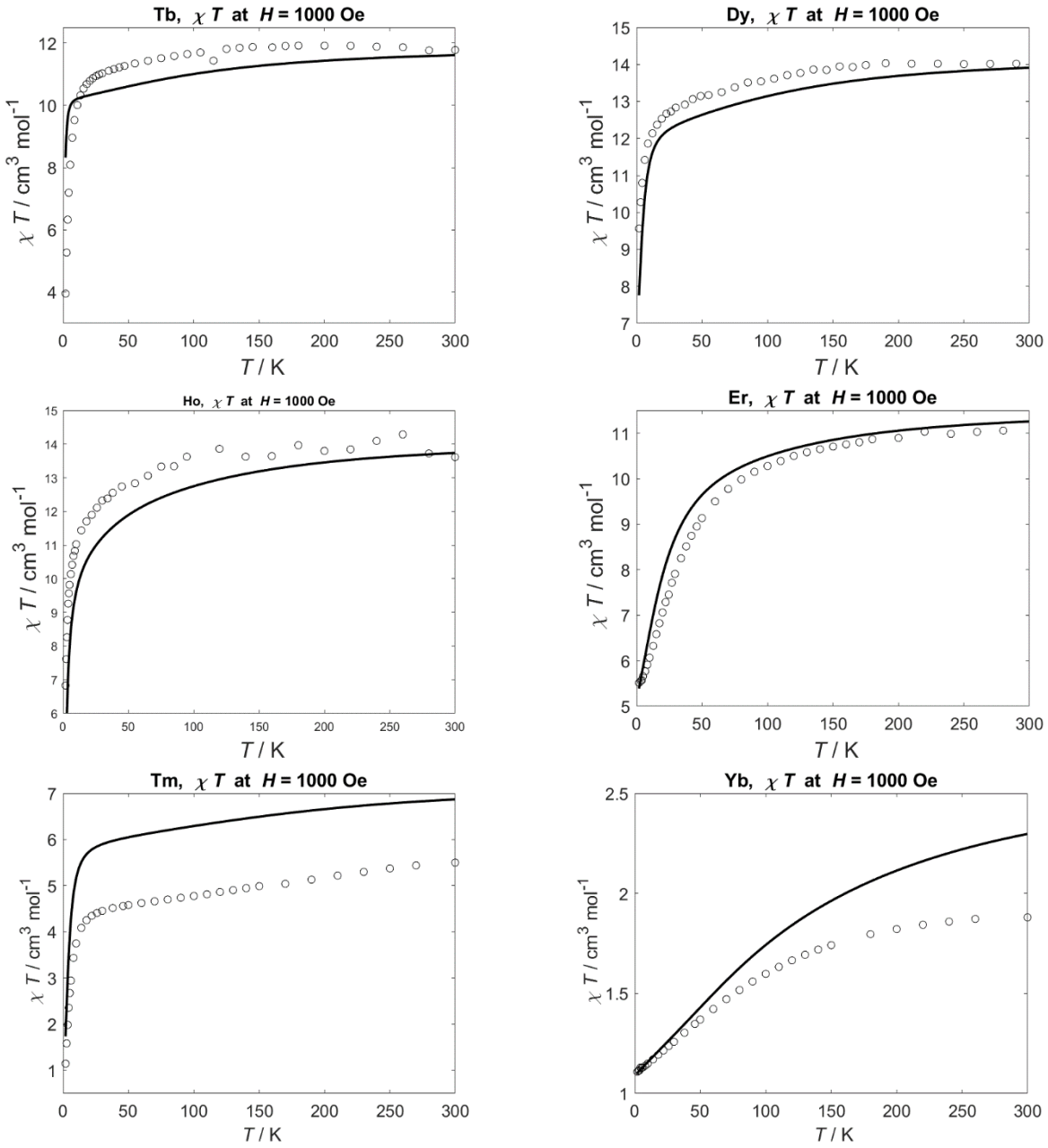

Figure S14. χT vs T curves (symbols) and *ab initio* simulations (black lines).

8. Energy level splitting and composition

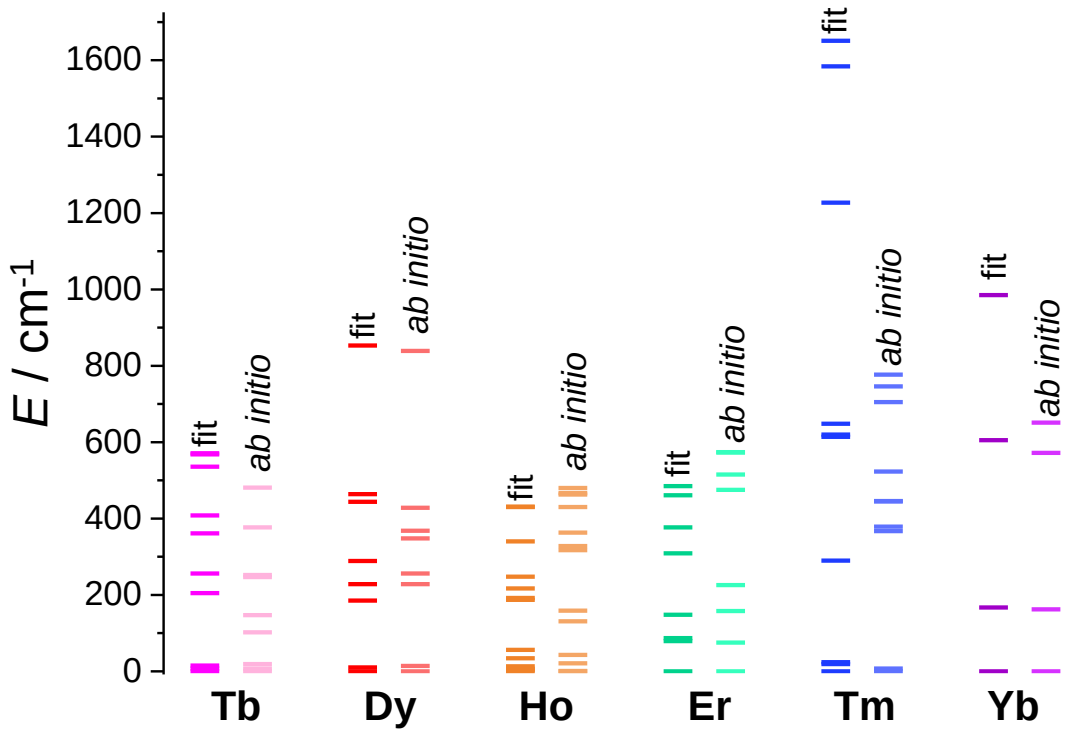

Figure S15. Energy level splitting of the ground multiples of all studied anisotropic derivatives.

Fitted eigenvalues and eigenvectors:

***E* / CM^{-1}**	**COMPOSITION**
0	0.01|+4⟩+0.98|0⟩+0.01|-4⟩
7.4	0.92|±1⟩+0.07|∓3⟩
19	0.5|±2⟩+0.5|∓2⟩
102	0.5|±2⟩+0.5|∓2⟩
147	0.93|±3⟩+0.07|∓1⟩
247	0.5|±4⟩+0.5|∓4⟩
252	0.5|±4⟩+0.5|∓4⟩
377	1|±5⟩
481.4	0.5|±6⟩+0.5|∓6⟩
481.5	0.5|±6⟩+0.5|∓6⟩

Table S9. Fitted energy and composition of the levels belonging to the J = 6 ground state of **Tb**.

***E* / CM^{-1}**	**COMPOSITION**
0	0.25|±7/2⟩+0.53|∓1/2⟩+0.22|∓9/2⟩
10	0.02|±13/2⟩+0.34|±5/2⟩+0.48|∓3/2⟩+0.17|∓11/2⟩
185	0.08|±13/2⟩+0.20|±5/2⟩+0.71|∓11/2⟩

228	0.38|±7/2⟩+0.01|∓1/2⟩+0.61|∓9/2⟩
289	0.07|±11/2⟩+0.09|±3/2⟩+0.84|∓13/2⟩
444	0.17|±9/2⟩+0.46|±1/2⟩+0.37|∓7/2⟩
464	0.05|±11/2⟩+0.43|±3/2⟩+0.46|∓5/2⟩+0.06|∓13/2⟩
853	1|±15/2⟩

Table S10. Fitted energy and composition of the levels belonging to the J = 15/2 ground state of **Dy**.

E **/ CM^{-1}**	**COMPOSITION**
0	0.02|±8⟩+0.45|±4⟩+0.07|0⟩+0.45|∓4⟩+0.02|∓8⟩
3.7	0.18|±5⟩+0.12|±1⟩+0.62|∓3⟩+0.08|∓7⟩
6.72	0.15|±6⟩+0.35|±2⟩+0.35|∓2⟩+0.15|∓6⟩
13.0	0.02|±8⟩+0.48|±4⟩+0.48|∓4⟩+0.02|∓8⟩
33.9	0.04|±7⟩+0.24|±3⟩+0.08|∓1⟩+0.64|∓5⟩
55.8	0.24|±6⟩+0.26|±2⟩+0.26|∓2⟩+0.24|∓6⟩
187.4	0.03|±4⟩+0.93|0⟩+0.03|∓4⟩
192.3	0.01|±7⟩+0.02|±3⟩+0.79|∓1⟩+0.18|∓5⟩
217.4	0.35|±6⟩+0.15|±2⟩+0.15|∓2⟩+0.35|∓6⟩
248.3	0.26|±6⟩+0.24|±2⟩+0.24|∓2⟩+0.26|∓6⟩
340.3	0.87|±7⟩+0.13|±3⟩
430.1	0.48|±8⟩+0.02|±4⟩+0.02|∓4⟩+0.48|∓8⟩
430.5	0.48|±8⟩+0.02|±4⟩+0.02|∓4⟩+0.48|∓8⟩

Table S11. Fitted energy and composition of the levels belonging to the J = 8 ground state of **Ho**.

E **/ CM^{-1}**	**COMPOSITION**
0	0.03|±11/2⟩+0.06|±3/2⟩+0.15|∓5/2⟩+0.77|∓13/2⟩
79	0.13|±9/2⟩+0.55|±1/2⟩+0.15|∓7/2⟩+0.17|∓15/2⟩
87	0.11|±13/2⟩+0.01|±5/2⟩+0.37|∓3/2⟩+0.51|∓11/2⟩
148	0.07|±9/2⟩+0.17|±1/2⟩+0.1|∓7/2⟩+0.74|∓15/2⟩
309	0.07|±13/2⟩+0.31|±5/2⟩+0.24|∓3/2⟩+0.38|∓11/2⟩
377	0.05|±15/2⟩+0.31|±7/2⟩+0.04|∓1/2⟩+0.60|∓9/2⟩
461	0.09|±11/2⟩+0.33|±3/2⟩+0.52|∓5/2⟩+0.05|∓15/2⟩
485	0.20|±9/2⟩+0.24|±1/2⟩+0.53|∓7/2⟩+0.04|∓15/2⟩

Table S12. Fitted energy and composition of the levels belonging to the J = 15/2 ground state of **Er**.

E **/ CM^{-1}**	**COMPOSITION**
0	0.44|±6⟩+0.06|±2⟩+0.06|∓2⟩+0.44|∓6⟩
19	0.44|±6⟩+0.06|±2⟩+0.06|∓2⟩+0.44|∓6⟩
24	0.98|±3⟩+0.02|∓1⟩
290	0.06|±6⟩+0.44|±2⟩+0.44|∓2⟩+0.06|∓6⟩
614	0.5|±4⟩+0.5|∓4⟩
620	0.5|±4⟩+0.5|∓4⟩
648	0.01|±6⟩+0.49|±2⟩+0.49|∓2⟩+0.01|∓6⟩
1227	0.01|±5⟩+0.97|±1⟩+0.01|∓3⟩
1584	0.99|0⟩
1651	0.98|±5⟩+0.01|±1⟩

Table S13. Fitted energy and composition of the levels belonging to the J = 6 ground state of **Tm**.

E / CM^{-1}	COMPOSITION
0	0.84|±5/2⟩+0.15|∓3/2⟩
305	0.90|±7/2⟩+0.10|∓1/2⟩
684	0.10|±7/2⟩+0.90|∓1/2⟩
711	0.84|±3/2⟩+0.15|∓5/2⟩

Table S14. Fitted energy and composition of the levels belonging to the J = 7/2 ground state of **Yb**.

Ab initio eigenvalues and eigenvectors

E / CM^{-1}	COMPOSITION
0	0.92|0⟩+0.08|±4⟩
7	0.83|±1⟩+0.15|±3⟩
7	0.83|±1⟩+0.15|±3⟩
15	1.00|±2⟩
205	0.99|±2⟩
256	0.84|±3⟩+0.15|±1⟩
256	0.84|±3⟩+0.15|±1⟩
361	1|±4⟩
408	0.92|±4⟩+0.08|0⟩
536	0.98|±5⟩+0.02|±1⟩
536	0.98|±5⟩+0.02|±1⟩
568	1|±6⟩
571	0.99|±6⟩+0.01|±2⟩

Table S16. *Ab initio* energy and composition of the levels belonging to the J = 6 ground state of **Tb**.

E / CM^{-1}	COMPOSITION
0	0.52|±3/2⟩+0.44|±5/2⟩+0.03|±11/2⟩+0.01|±13/2⟩
14	0.60|±1/2⟩+0.29|±7/2⟩+0.11|±9/2⟩
228	0.64|±9/2⟩+0.35|±7/2⟩+0.01|±1/2⟩
256	0.71|±11/2⟩+0.19|±5/2⟩+0.05|±13/2⟩+0.05|±1/2⟩
348	0.39|±13/2⟩+0.23|±11/2⟩+0.26|±3/2⟩+0.11|±5/2⟩
368	0.40|±1/2⟩+0.35|±7/2⟩+0.25|±9/2⟩
428	0.55|±13/2⟩+0.26|±5/2⟩+0.16|±13/2⟩+0.03|±11/2⟩
839	0.99|±15/2⟩+0.01|±7/2⟩

Table S17. *Ab initio* energy and composition of the levels belonging to the J = 15/2 ground state of **Dy**.

E / CM^{-1}	COMPOSITION
0	0.70|±3⟩+0.13|±7⟩+0.12|±1⟩+0.04|±5⟩
0.3	0.70|±3⟩+0.13|±7⟩+0.12|±1⟩+0.04|±5⟩
1.3	0.80|±2⟩+0.20|±6⟩
21	0.82|±4⟩+0.12|±8⟩+0.06|0⟩
43	0.86|±4⟩+0.14|±8⟩
131	0.77|±5⟩+0.12|±1⟩+0.7|±3⟩+0.3|±7⟩
131	0.77|±5⟩+0.12|±1⟩+0.7|±3⟩+0.3|±7⟩
159	0.52|±6⟩+0.48|±2⟩
317	0.92|0⟩+0.06|±8⟩+0.03|±4⟩
328	0.72|±1⟩+0.19|±5⟩+0.07|±7⟩+0.02|±3⟩
328	0.72|±1⟩+0.19|±5⟩+0.07|±7⟩+0.02|±3⟩

363	0.80|±6⟩+0.20|±2⟩
430	0.51|±2⟩+0.49|±6⟩
463	0.86|±8⟩+0.14|±4⟩
467	0.82|±8⟩+0.15|±4⟩+0.03|±0⟩
480	0.76|±7⟩+0.20|±3⟩+0.03|±1⟩
480	0.76|±7⟩+0.20|±3⟩+0.03|±1⟩

Table S18. *Ab initio* energy and composition of the levels belonging to the J = 8 ground state of **Ho**.

***E* / CM^{-1}**	**COMPOSITION**
0	0.70|±13/2⟩+0.23|±5/2⟩+0.05|±3/2⟩+0.02|±11/2⟩
75	0.82|±15/2⟩+0.14|±7/2⟩+0.04|±1/2⟩
158	0.49|±3/2⟩+0.42|±11/2⟩+0.09|±13/2⟩
226	0.82|±1/2⟩+0.12|±9/2⟩+0.06|±15/2⟩
475	0.40|±11/2⟩+0.29|±5/2⟩+0.19|±3/2⟩+0.11|±13/2⟩
515	0.81|±9/2⟩+0.10|±7/2⟩+0.08|±1/2⟩+0.02|±15/2⟩
573	0.75|±7/2⟩+0.10|±15/2⟩+0.07|±1/2⟩+0.07|±9/2⟩
574	0.48|±5/2⟩+0.26|±3/2⟩+0.16|±1/2⟩+0.10|±13/2⟩

Table S19. *Ab initio* energy and composition of the levels belonging to the J = 15/2 ground state of **Er**.

***E* / CM^{-1}**	**COMPOSITION**
0	0.96|±6⟩+0.04|±2⟩
7	0.99|±6⟩+0.01|±2⟩
367	0.37|±5⟩+0.34|±3⟩+0.29|±1⟩
367	0.37|±5⟩+0.34|±3⟩+0.29|±1⟩
379	0.96|±2⟩+0.04|±6⟩
445	0.61|±5⟩+0.32|±3⟩+0.07|±1⟩
445	0.61|±5⟩+0.32|±3⟩+0.07|±1⟩
446	0.71|±4⟩+0.29|0⟩
523	1.00|±4⟩
705	0.71|0⟩+0.29|±4⟩
746	0.64|±1⟩+0.34|±3⟩+0.02|±5⟩
746	0.64|±1⟩+0.34|±3⟩+0.02|±5⟩
777	0.99|±2⟩+0.01|±6⟩

Table S20. *Ab initio* energy and composition of the levels belonging to the J = 6 ground state of **Tm**.

***E* / CM^{-1}**	**COMPOSITION**
0	0.85|±5/2⟩+0.15|±3/2⟩
162	0.98|±7/2⟩+0.02|±1/2⟩
572	0.85|±3/2⟩+0.15|±5/2⟩
651	0.99|±1/2⟩+0.01|±7/2⟩

Table S21. *Ab initio* energy and composition of the levels belonging to the J = 7/2 ground state of **Yb**.

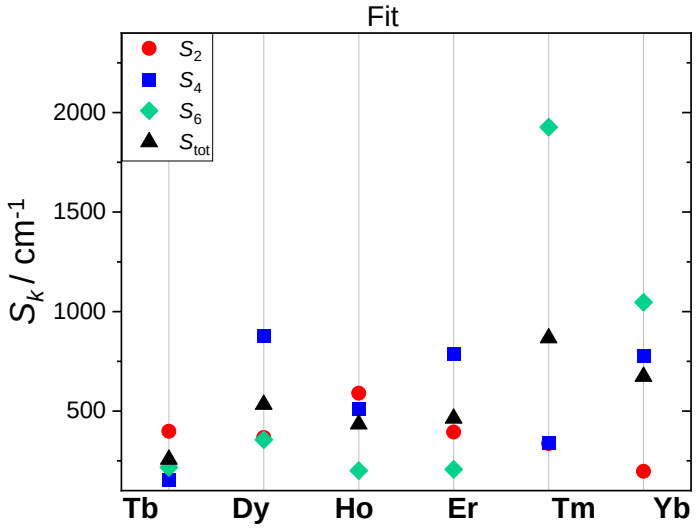

Figure S16. CF strength obtained for all the studied anisotropic derivatives.

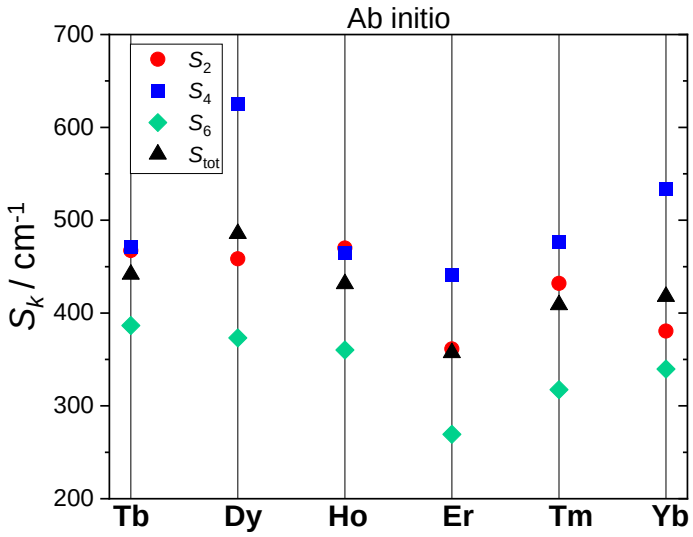

Figure S17. CF strength obtained for all the studied anisotropic derivatives.

9. Magnetic measurements: magnetic moment vs temperature

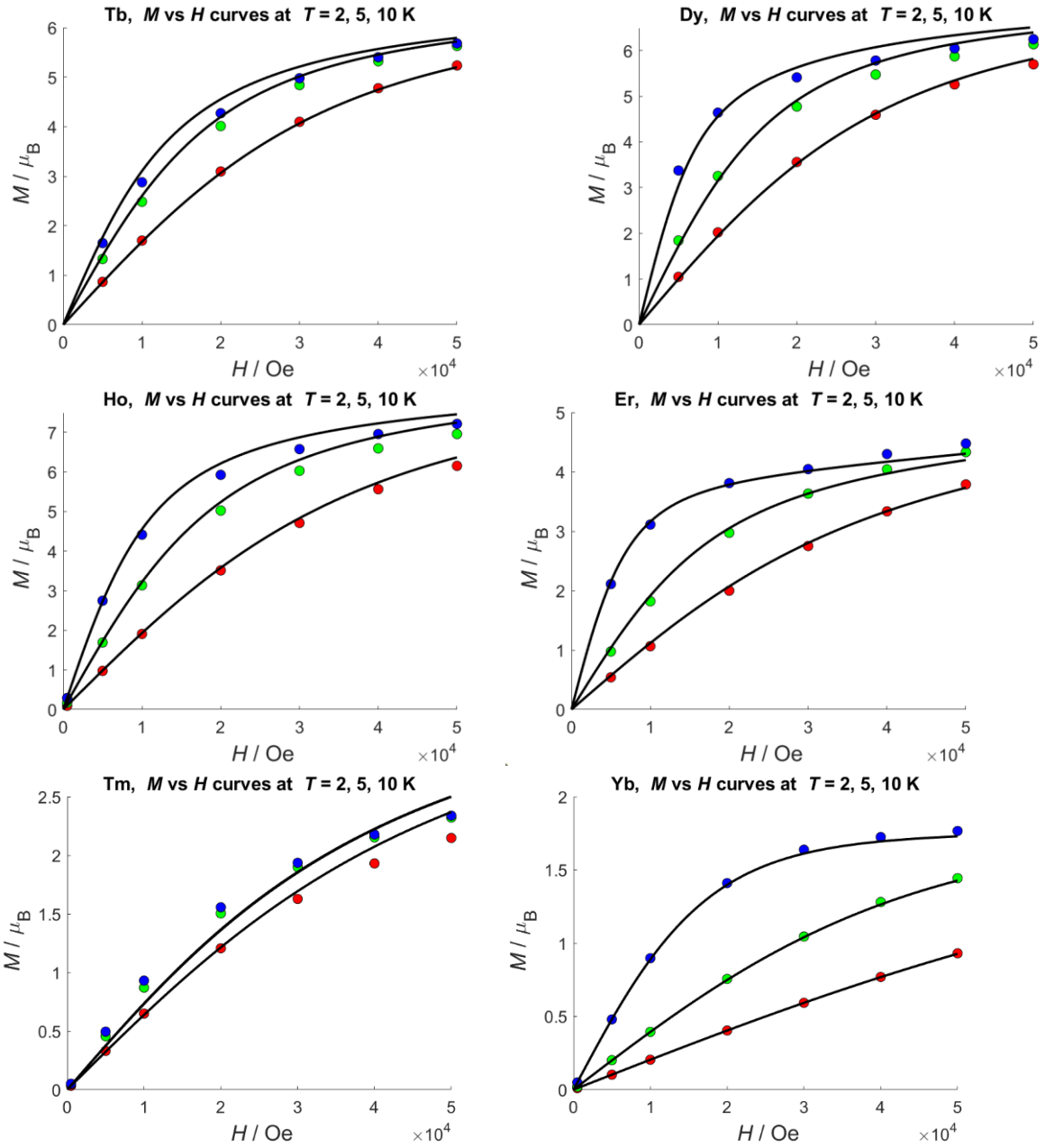

Figure S18. *M* vs *H* curves (symbols) and best fit (black lines).

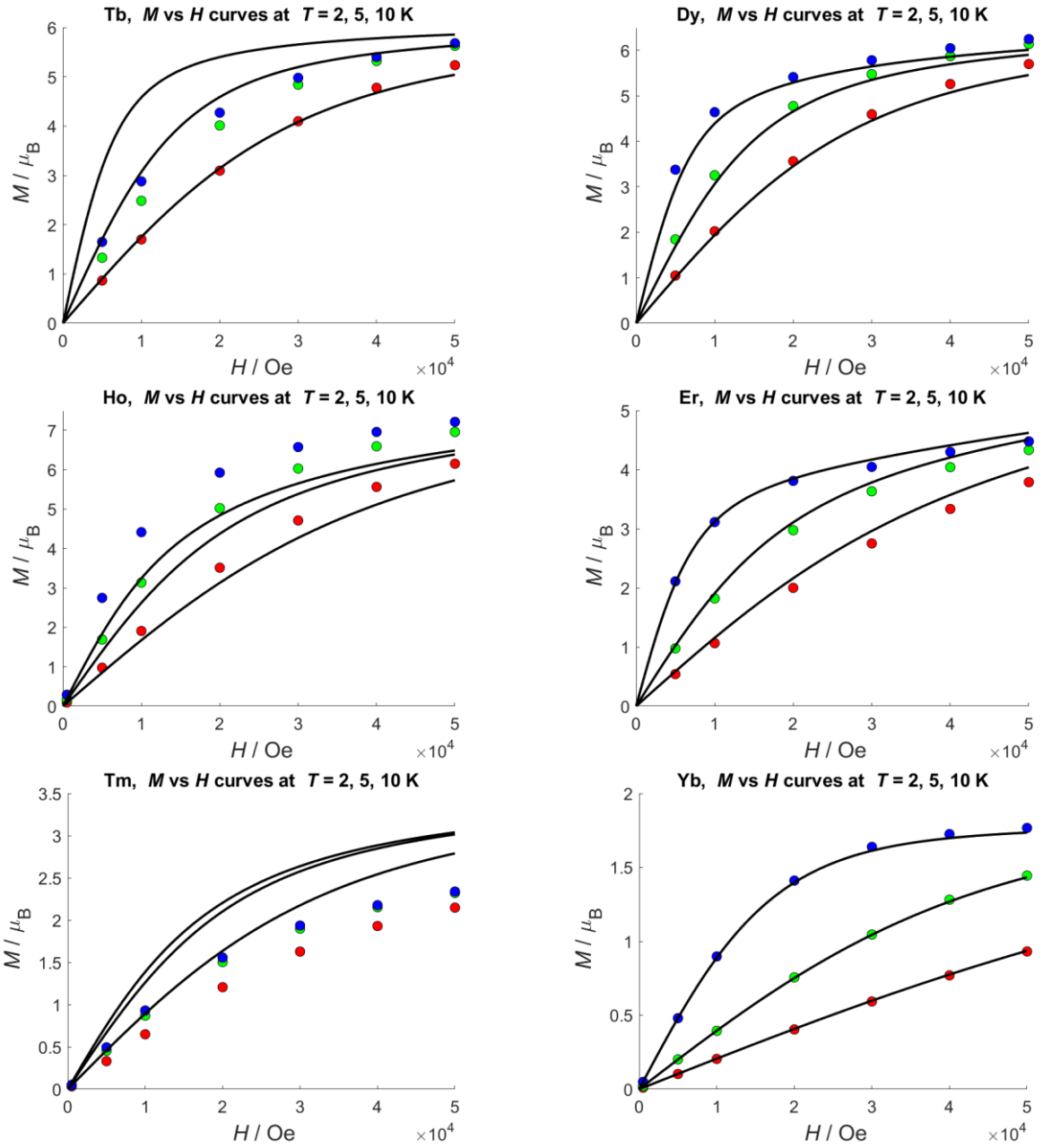

Figure S19. *M* vs *H* curves (symbols) and *ab initio* simulations(black lines).

10. Nephelauxetic effect

	E^3 CASSCF+NEVPT2 (cm^{-1})			SOC parameter ζ CASSCF+NEVPT2 (cm^{-1})		
	LnDOTA	**Free Ion**	**Nephelauxetic ratio**	**LnDOTA**	**Free Ion**	**Nephelauxetic ratio**
Tb^{3+}	-	-	-	1741.4	1752.3	0.9938
Dy^{3+}	609.6	620.9	0.9818	1933.9	1944.8	0.9944
Ho^{3+}	631.4	643.4	0.9814	2145.3	2156.4	0.9949
Er^{3+}	654.3	664.9	0.9841	2372.0	2383.1	0.9953
Tn^{3+}	677.0	686.6	0.9860	2619.3	2630.5	0.9957
Yb^{3+}	-	-	-	2876.5	2887.6	0.9962

Table S22. Computed Racah E^3 parameter and SOC constant ζ for all LnDOTA complexes and the corresponding free ions through AILFT approach.

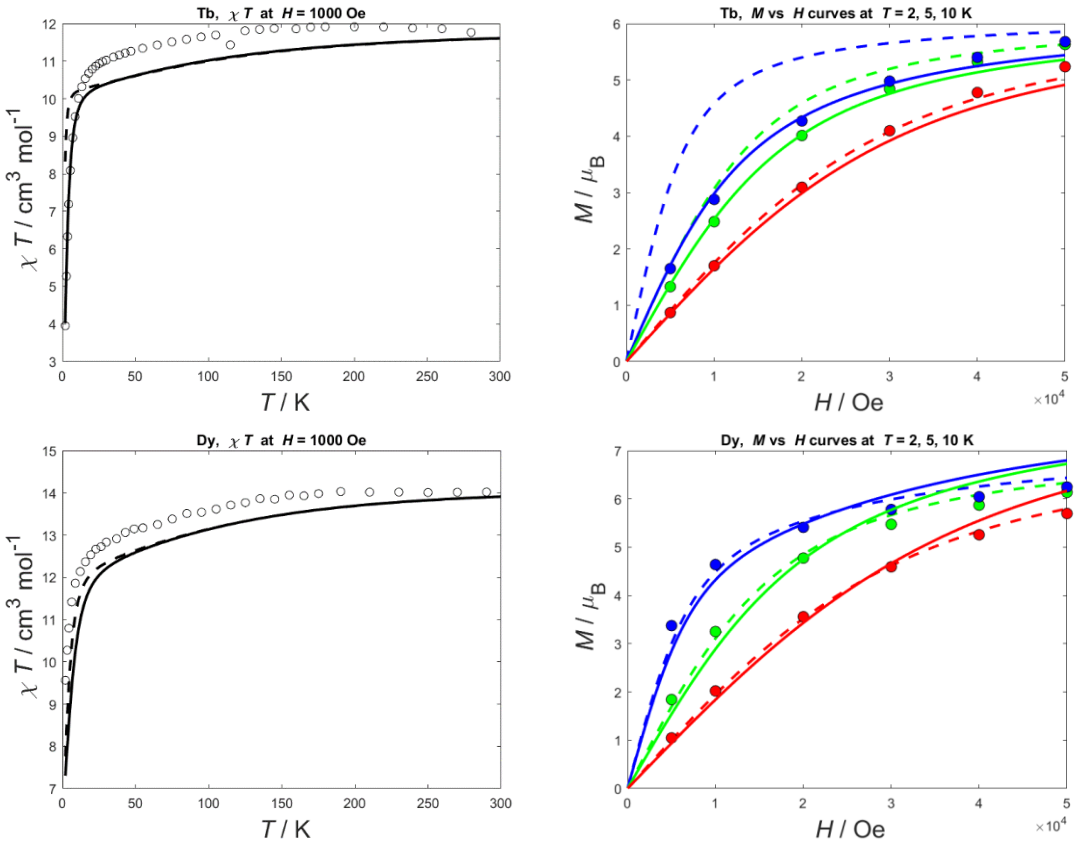

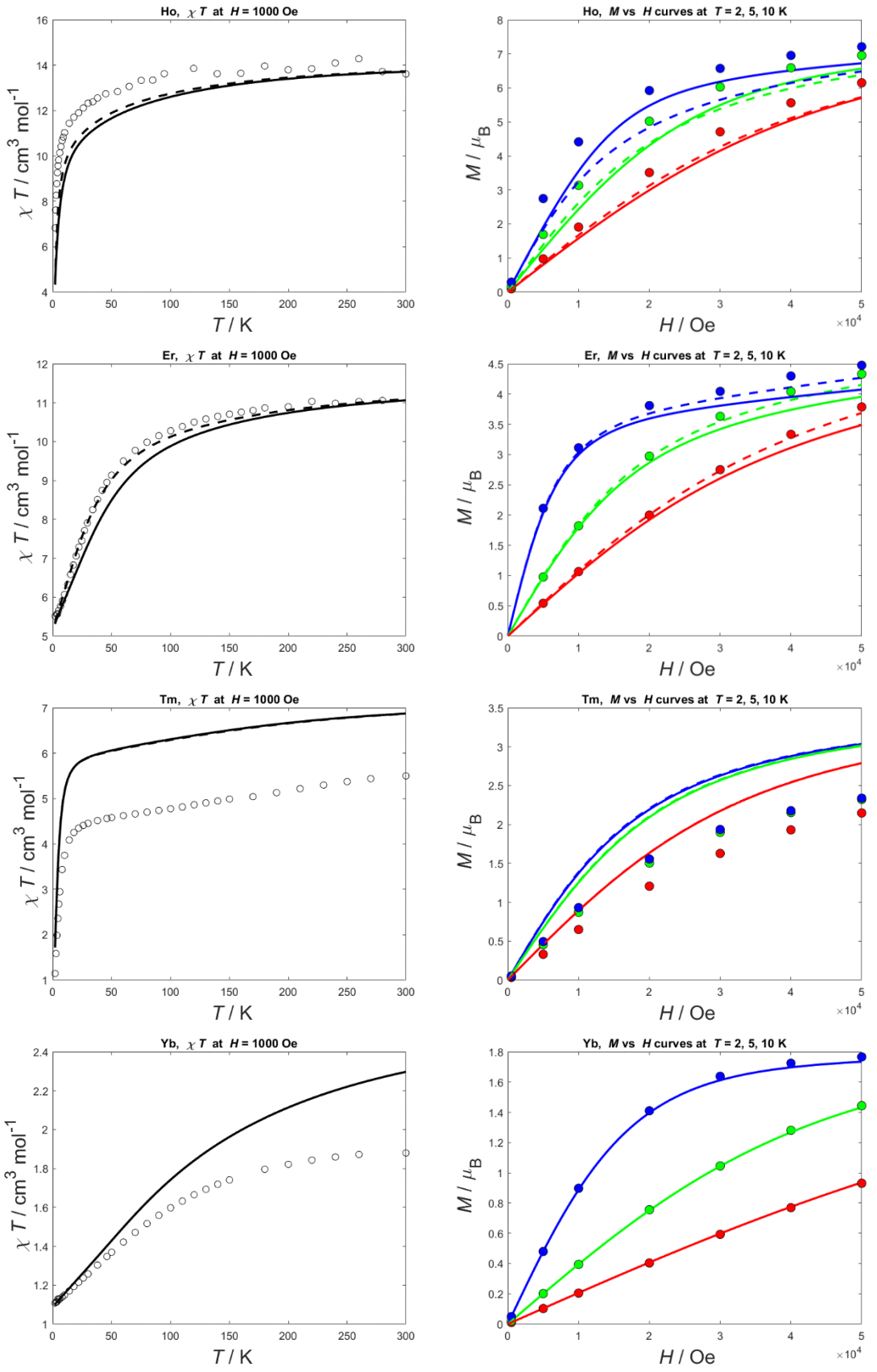

Figure S20. Effect of the inclusion of the 8th order parameters in the magnetic data. The symbols are the experimental points. The solid lines are the simulations with the inclusion of the 8th order

parameters and the dashed lines are the simulations with the parameters up to the 6th order. In the case of **Yb** we see no effect.

Energy (cm^{-1})	Component	Values	a	b	c
0	g_x	0.540	-0.093415	-0.029380	0.995194
	g_y	1.517	0.412041	-0.911089	0.011779
	g_z	17.434	0.906364	0.411161	0.097215
30	g_x	0.309	-0.036573	-0.018923	0.999152
	g_y	1.773	0.927200	0.372317	0.040990
	g_z	17.465	-0.372777	0.927913	0.003929

Table S23. *Ab initio* computed energy, *g*-tensor values and orientations of the ground and first excited Kramers' doublets for **Dy+H_2O** model. The c axis is parallel to the C_4 axis of the molecule.

11. Anisotropy of the complexes

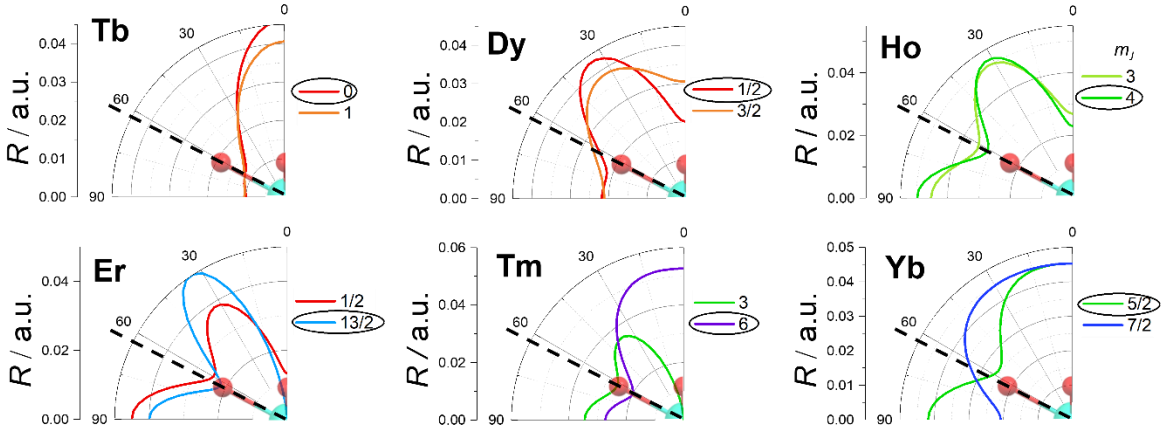

Figure S21. Electron density (*R*) of the two most stabilized m_J states (coloured lines) superimposed on the molecular structures of the complexes. The dotted lines emphasize the position of the carboxylic coordinating oxygen atoms. The most stabilized m_J is evidenced with a black circle.

12. Ac measurements

Oblate ions

Tb does not show any slow relaxation, as expected from its singlet, $m_J = 0$, ground state.

Dy loses its zero-field SMM behaviour compared to the hydrated analogue and does not show any sign of thermally activated relaxation processes, as expected from the change in magnetic anisotropy. A field scan at low temperature evidences two signals for the out of phase component of the magnetic susceptibility at all the investigated fields (Figure S22). The maxima of these two contributions to the magnetization relaxation clearly move to lower frequencies by increasing the applied magnetic field indicating that field-dependent relaxation pathways are active. At a field of $H = 5000$ Oe, the relaxation times for the two processes are essentially constant ($\tau_1 \approx 0.5$ s, $\tau_2 \approx 8\ 10^{-3}$ s) at all investigated temperatures (Figure S23) suggesting a dominance of QT relaxation pathway. Although not directly comparable because being recorded at an applied field, the dc data show a dc susceptibility much larger than the difference between the isothermal and adiabatic susceptibility extracted from the fits (Figure S24). This suggests that only a minor fraction of the molecules (< 25 %) is slowly relaxing, corroborating our magnetic anisotropy assignment.

The **Ho** derivative is the only non-Kramers ion showing in-field slow relaxation and its out-of-phase component of the magnetic susceptibility behaves similarly to **Dy**. The broad out of phase component that is observed can be justified by the presence of more than one contribution to the magnetization relaxation (Figure S26). The temperature scan at an optimum field of $H = 4000$ Oe shows a major active process ($\tau \approx 0.8$ s) and a minor one ($\tau \approx 7\ 10^{-3}$ s) in the entire temperature range (Figure S27). Only < 30% of molecules follow the slow relaxation, even summing up both processes (Figure S28). The absence of temperature dependence suggests QT as the preferred relaxation pathway. From both experimental modelling and *ab initio* calculations the ground state of this complex is a singlet and can therefore not be uniquely responsible for the observed behaviour. However, the first excited doublet (predominantly composed by $|\pm3\rangle$ according to both ab initio calculations and experimental fit) lies less than 4 cm^{-1} from the ground state, as detected via INS. This doublet is significantly populated at low temperature (Boltzmann population ≈ 12 % at $T = 2$ K and $H = 4000$ Oe). Therefore, we attribute the magnetization dynamics to the relaxation between these states.

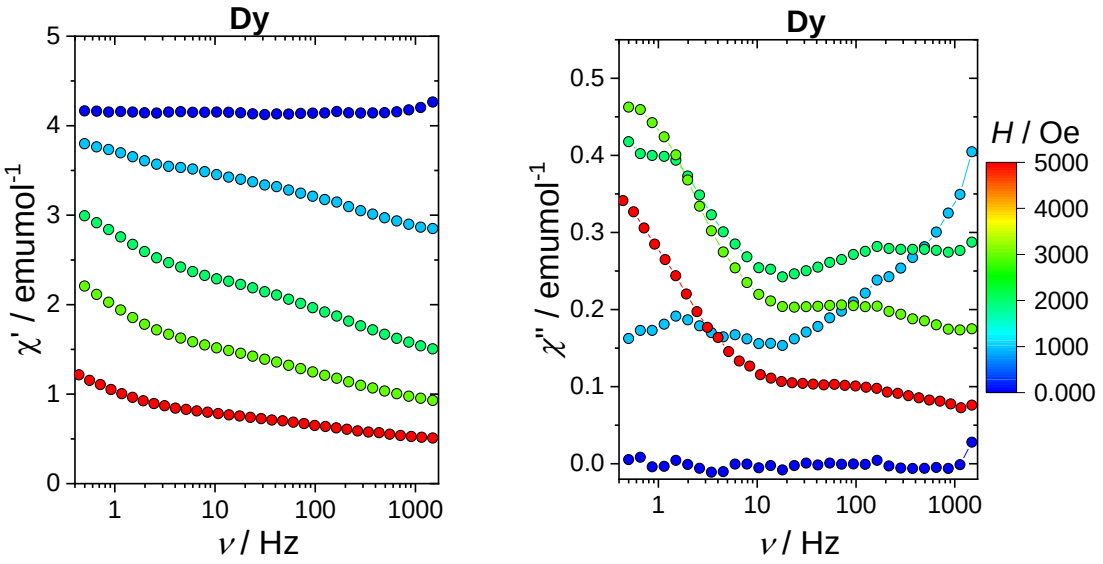

Figure S22. In phase and out of phase ac magnetic susceptibility of **Dy** recorded at T = 2 K and various fields.

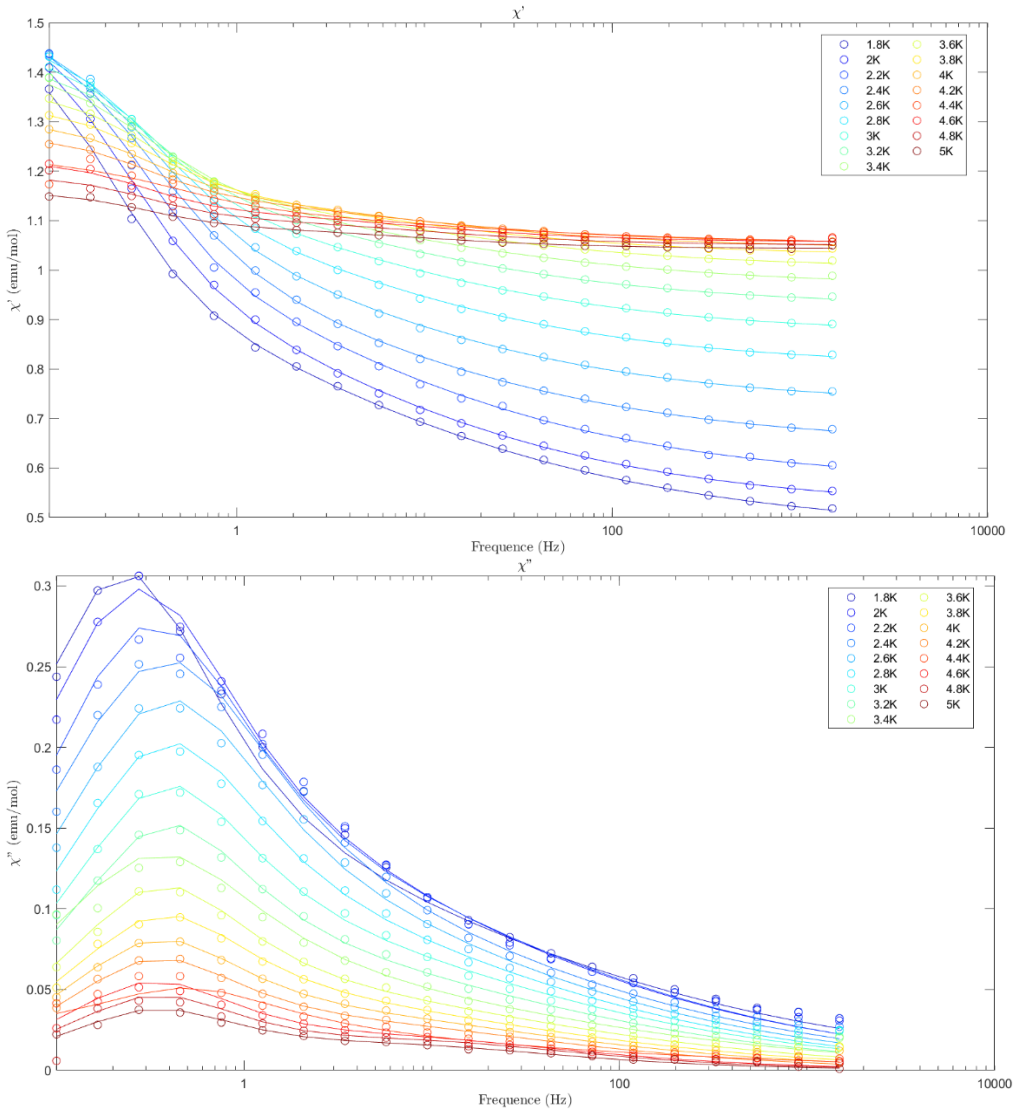

Figure S23. In phase and out of phase ac magnetic susceptibility of **Dy** recorded at *H* = 5000 Oe and various temperatures.

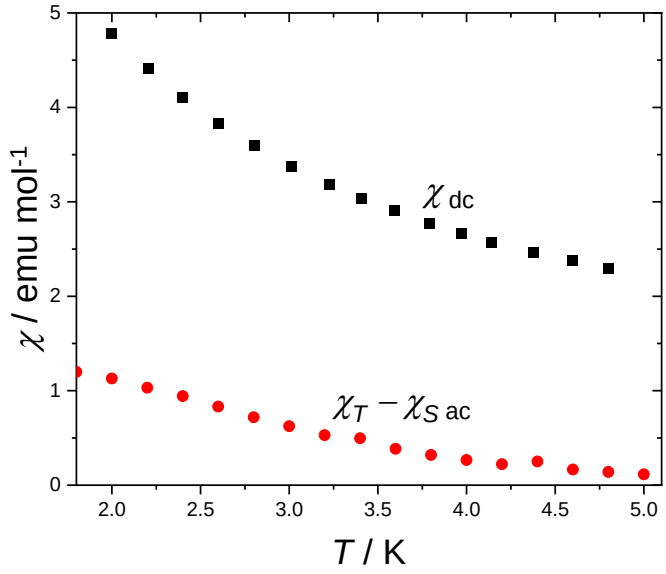

Figure S24. Comparison between the dc (black dots, *H* = 1000 Oe) and ac (red dots, *H* = 5000 Oe) susceptibility. Assuming linear behaviour of *M* vs *H* at both applied fields, the two values are expected to be equal for 100% of molecules slowly relaxing.

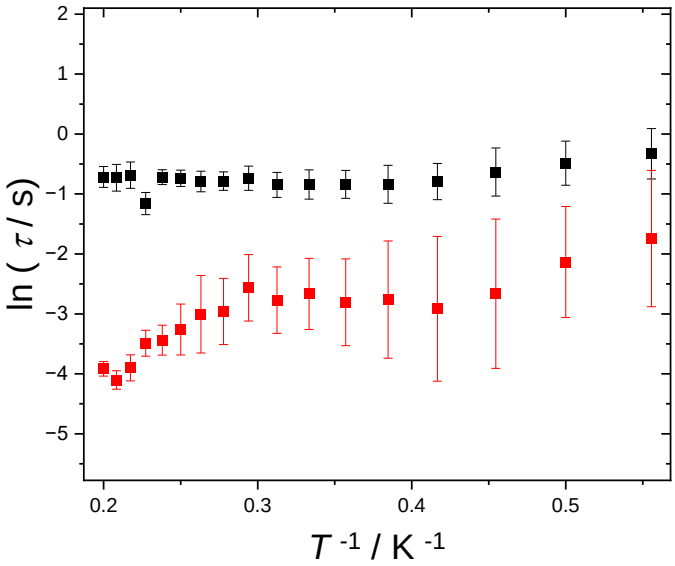

Figure S25. Relaxation times of the two relaxation processes (red and black symbols) extracted from the fit of the temperature scan of **Dy**.

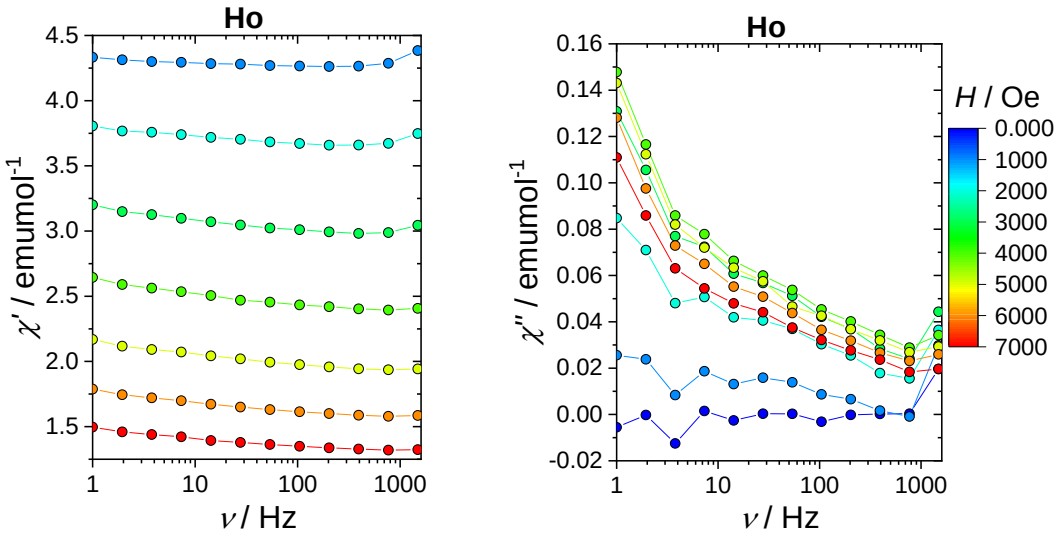

Figure S26. In phase and out of phase ac magnetic susceptibility of **Ho** recorded at T = 2 K and various fields.

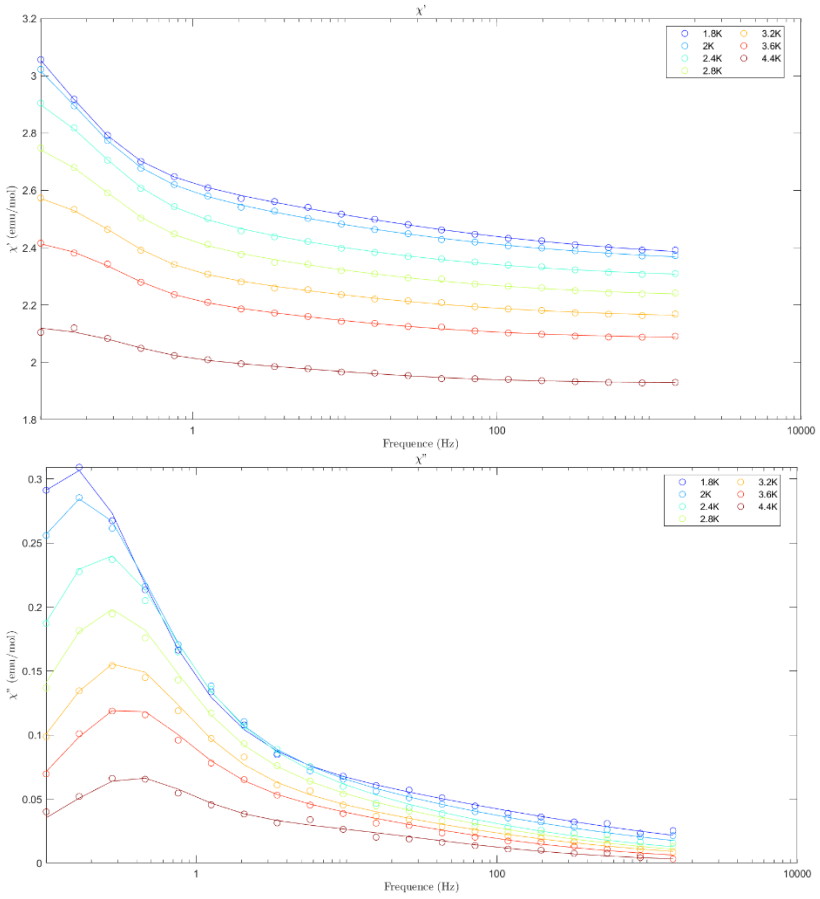

Figure S27. In phase and out of phase ac magnetic susceptibility of **Ho** recorded at H = 4000 Oe and various temperatures.

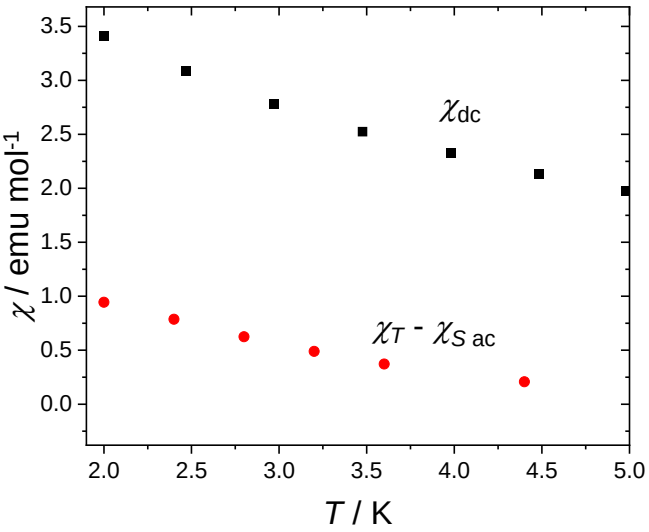

Figure S28. Comparison between the dc (black dots, *H* = 1000 Oe) and ac (red dots, *H* = 4000 Oe) susceptibility. Assuming linear behaviour of *M* vs *H* at both applied fields, the two values are expected to be equal for 100% of molecules slowly relaxing.

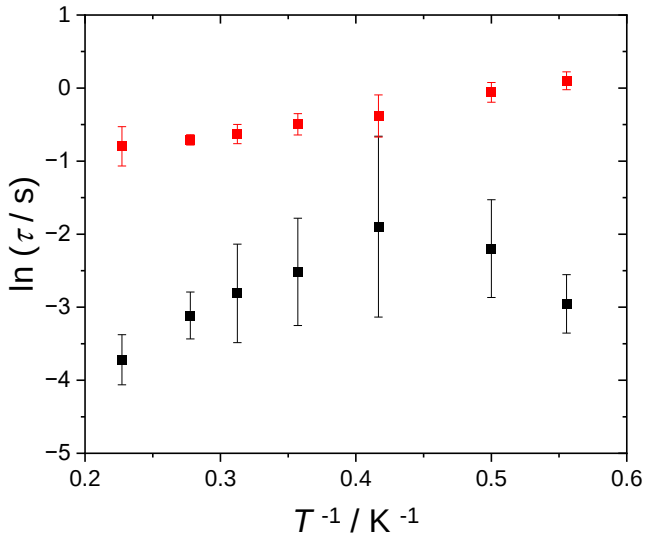

Figure S29. Relaxation times of the two relaxation processes (red and black symbols) extracted from the fit of the temperature scan of **Ho**.

Prolate ions

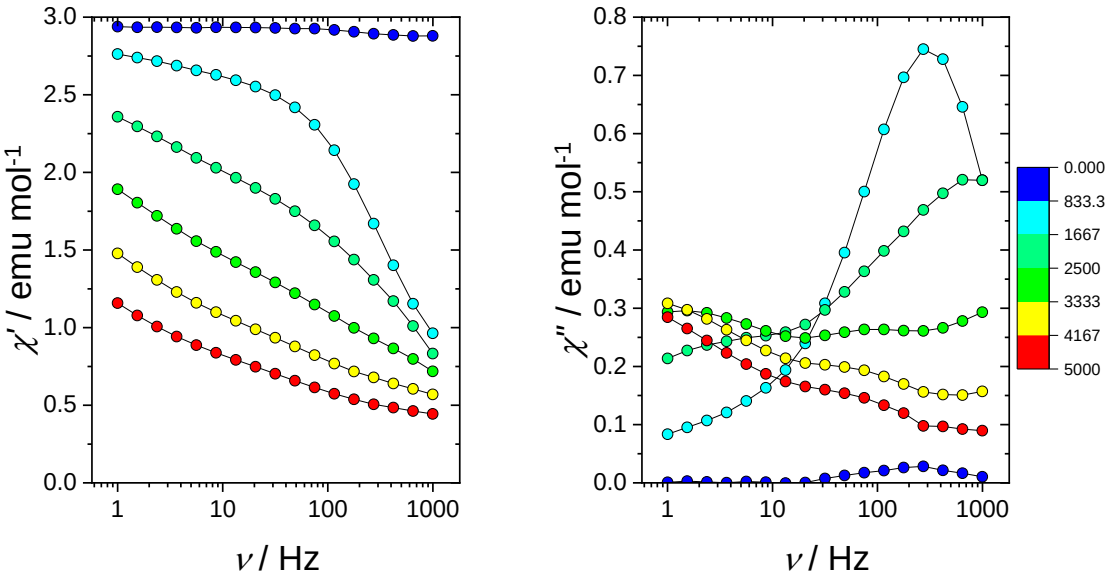

Figure S30. In phase and out of phase ac magnetic susceptibility of **Er** recorded at T = 2 K and various fields.

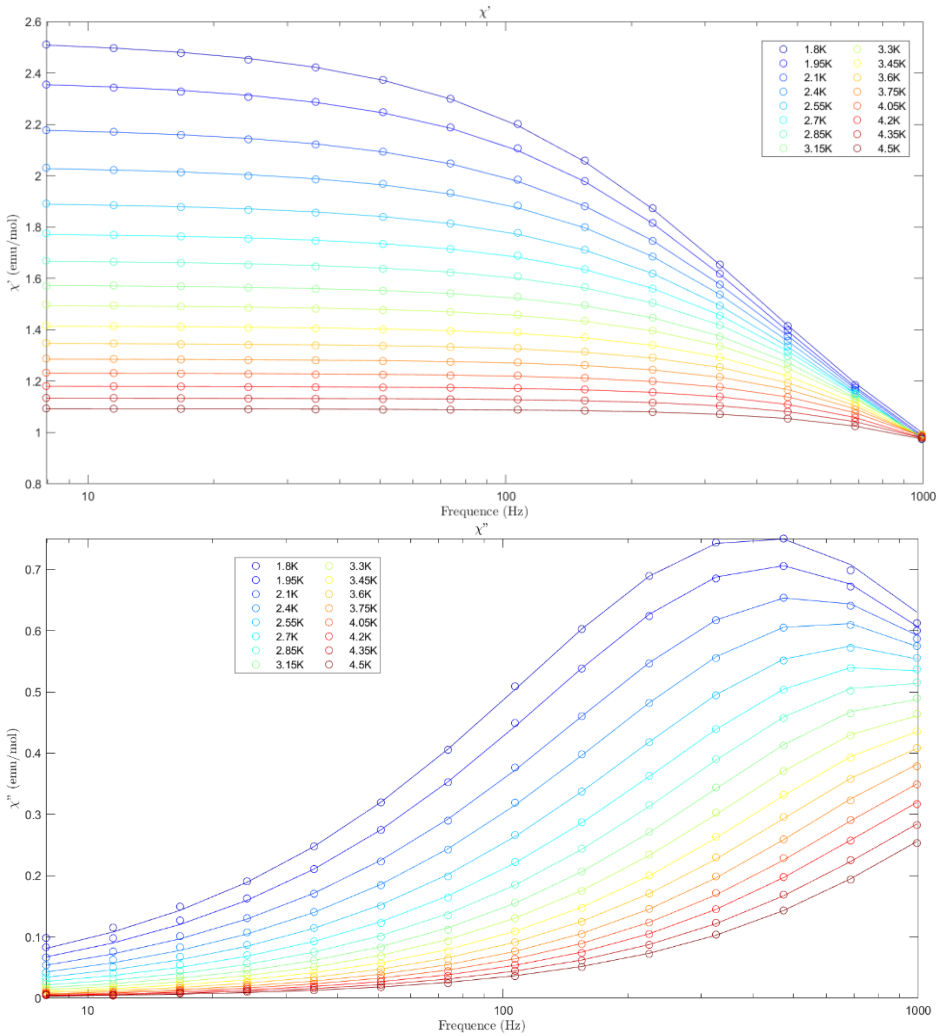

Figure S31. In phase (left) and out of phase (right) ac magnetic susceptibility of **Er** recorded at H = 1000 Oe and various temperatures.

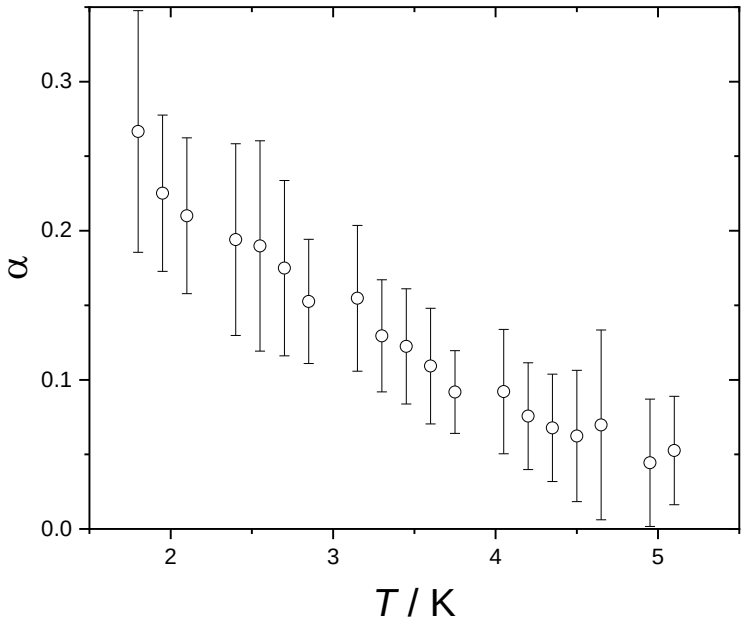

Figure S32. Distribution of the relaxation time associated with the slow relaxation recorded for **Er**.

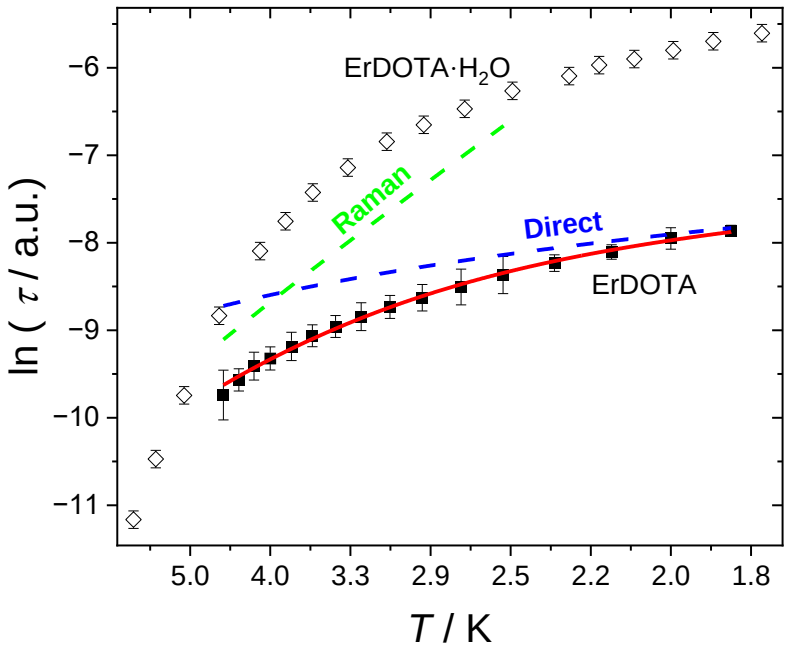

Figure S33. Relaxation time of **Er** at H = 1000 Oe. The squares are experimental points with their error bars. The red line is the best fit obtained by combining direct (blue line), Raman (green line). The empty diamonds are the relaxation times recorded on ErDOTA·H_2O.

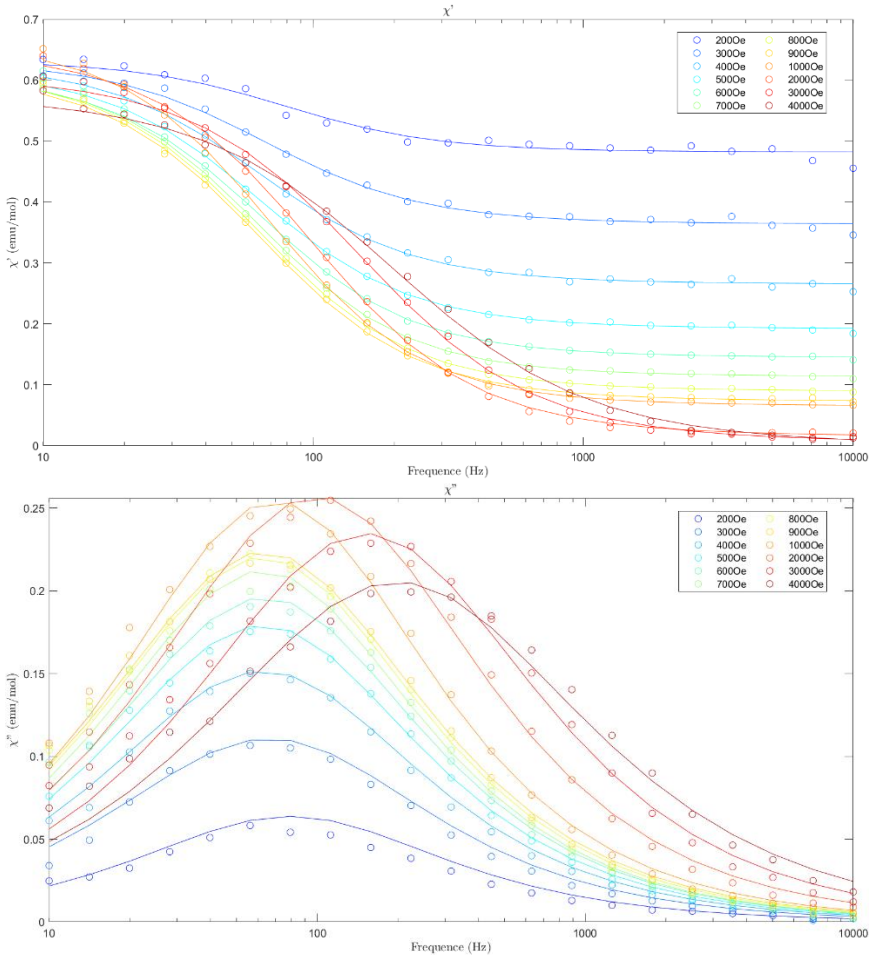

Figure S34. In phase and out of phase ac magnetic susceptibility of **Yb** recorded at *T* = 2 K and various fields.

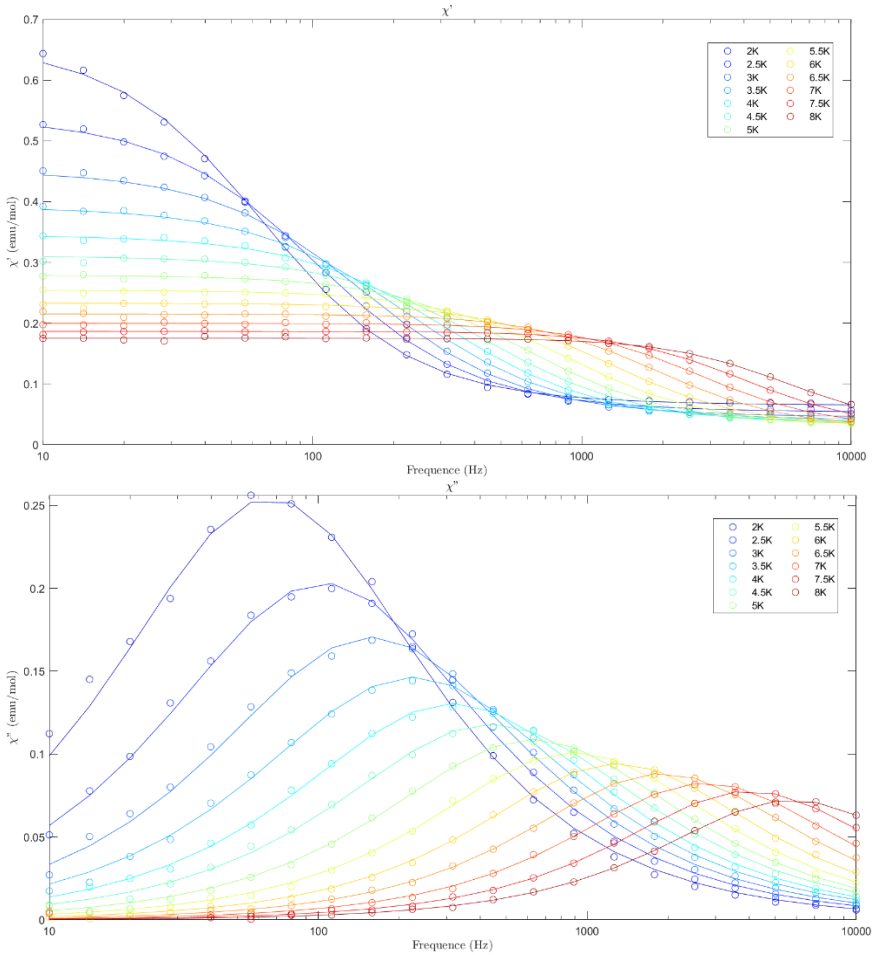

Figure S35. In phase and out of phase ac magnetic susceptibility of **Yb** recorded at *H* = 1000 Oe and various temperatures.

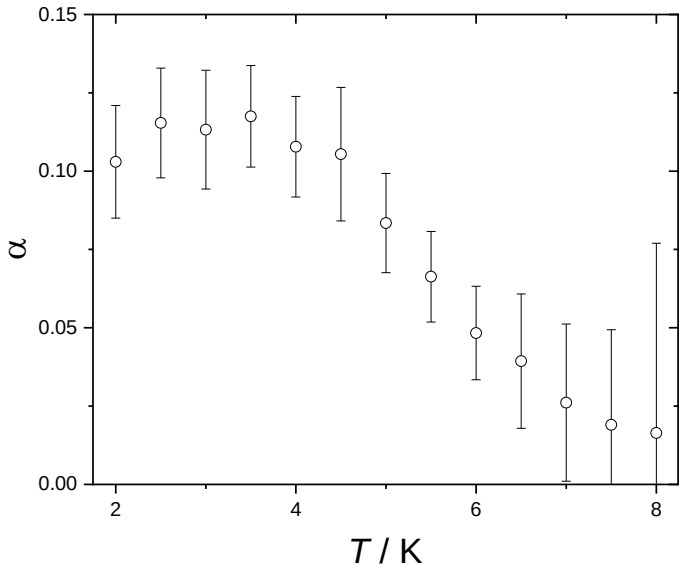

Figure S36. Distribution of the relaxation time associated with the slow relaxation recorded for **Yb**.

References

1. M. Briganti, E. Lucaccini, L. Chelazzi, S. Ciattini, L. Sorace, R. Sessoli, F. Totti and M. Perfetti, *J. Am. Chem. Soc.*, 2021, **143**, 8108-8115.
2. F. Neese, F. Wennmohs, U. Becker and C. Riplinger, *J. Chem. Phys.*, 2020, **152**, 224108.
3. D. Aravena, F. Neese and D. A. Pantazis, *J. Chem. Theory Comput.*, 2016, **12**, 1148-1156.
4. F. Weigend and R. Ahlrichs, *Phys. Chem. Chem. Phys.*, 2005, **7**, 3297-3305.
5. F. Neese, F. Wennmohs, A. Hansen and U. Becker, *Chem. Phys.*, 2009, **356**, 98-109.
6. I. Schapiro, K. Sivalingam and F. Neese, *J. Chem. Theory Comput.*, 2013, **9**, 3567-3580.
7. L. F. Chibotaru and L. Ungur, *J. Chem. Phys.*, 2012, **137**, 064112.
8. L. Ungur and L. F. Chibotaru, *Chem. Eur. J.*, 2017, **23**, 3708-3718.
9. A. Abragam and B. Bleaney, *Electron Paramagnetic Resonance of Transition Ions*, Dover, New York, 1986.
10. G. Stewart, *Hyperfine Interact.*, 1985, **23**, 1-16.